Stereo wave imaging from moving vessels: Practical use and applications

AlviseBenetazzo[a] FrancescoBarbariol[a] FilippoBergamasco[b] AndreaTorsello[b] SandroCarniel[a] MauroSclavo[a]

https://doi.org/10.1016/j.coastaleng.2015.12.008

Abstract

Stereo wave imaging of the sea surface elevation has become an effective instrumentation to gather small- and medium-range 3-D wind wave data. Indeed, fruitful applications of stereo techniques have provided new insights into directional wave spectra, space–time distributions of wave maxima, and small-scale wave statistics. So far, however, stereo systems have been deployed mainly on fixed structures (e.g. oceanographic platforms or lighthouses) in order to simplify the installation and maintenance procedures. Nonetheless, advances in stereo calibration and processing suggest that stereo deployments are also feasible onboard moving vessels, thus broadening the impact of these observations on the study of wind waves. In this context, this study aims at discussing how the stereo processing designed to gather reliable wave data from fixed structures should be managed to operate on a moving structure. In particular, estimate of stereo cameras orientation and position with respect to the mean sea plane is of utmost importance. We discuss this aspect by using a synthetic sea state and stereo data collected during an oceanographic campaign onboard a research vessel. Results suggest that, without complementary data sources for ship motion compensation, the sea surface elevation field should include at least about sixteen spatial (2-D) waves to gather a robust estimate of the mean sea plane and consequently realistic wave parameters (e.g. the significant wave height). In this respect, our results provide also insight into the uncertainty of estimates in case of a limited number of 2-D waves is collected by the stereo system. Finally, applications of stereo wave imaging on a moving structure are discussed, with particular emphasis on the collection of space–time wave fields for assessment of numerical models and operational wave observation onboard vessels.

1. Introduction

Statistical and spectral properties of wind waves are typically inferred from time records of sea surface elevations retrieved from instruments (like buoys or wave gauges) installed at fixed locations of the ocean. These observatories have provided unique datasets that have been extensively used over the years by generations of oceanographers and engineers. However, the information content of a single time series does not accurately predict the complete wave dynamics, which must be assumed as developing over the 2-D space as well as time (Boccotti, 2000). In this respect, in the recent past new classes of instrumentations (e.g. radars or lidars) have started to provide sufficient resolution and accuracy for measuring waves at different spatial scales, usually larger than some meters (Hwang et al., 2000, Nieto Borge, 2004, Romero and Melville, 2010). At smaller scales, however, where most of the air–sea exchanges occur, the optical systems (e.g. Jähne and Riemer, 1990, Zappa et al., 2008) have proved to gather sea elevations spatial data with higher accuracy. In this context, stereovision systems have started to gain credit as a tool to collect accurate 3-D fields of sea surface elevations. Starting from the pioneering studies of Schumacher (1939) and subsequent applications (e.g., Banner et al., 1989), thanks to a noticeable merging of image analysis techniques and available computational resources, stereo analysis has become only in the recent years a well explored technique for measuring sea waves remotely (Benetazzo et al., 2012, de Vries et al., 2011, Gallego et al., 2011, Kosnik and Dulov, 2011, Liu, 2013, Mironov et al., 2012). As mentioned, the added value of the stereo systems is the possibility to gather 3-D wave fields as they evolve in time, thus providing inputs to deepen the scientist knowledge on how the surface waves actually behave when they are treated as space–time fields (e.g. Banner et al., 2014, Benetazzo et al., 2015).

So far, however, stereo systems have been mostly installed on fixed platforms or piers over the sea. These conditions greatly ease the calibration and mounting procedure, as well as the entire processing necessary to get accurate sea waves information. Two stages have always been considered as critical when using stereo cameras at sea. Firstly, the computation of the so-called external parameters (Ma et al., 2004) that provide, for a given stereo setup, rotation and displacements between the cameras (generally two) is crucial for field applications in which it may be unfeasible to take apart or even physically access the device. Then, the pose (i.e. the orientation and position in 3-D space) of the stereo-camera system with respect to the mean sea surface must be accounted for to attain a proper space–time sea surface representation. For deployment on fixed structures, it has been verified (Benetazzo, 2006) that the mean sea plane can be accurately determined by a time-averaging procedure of the planes best-fitting the 3-D wave field mapped in the camera reference frame. When installing the stereo system on a moving structure, however, the 3-D mapping onto the sea reference is much more complicated, since this averaging is not feasible in a straightforward manner. A different strategy, therefore, must be adopted to transform the stereo 3-D data onto a reference system consistent with the horizontal mean sea plane. This topic was partially resolved, for instance, by Brandt et al. (2010) using the horizon visible in each frame to track the stereo cameras rotational motion, and by Schwendeman and Thomson (2015) who developed a horizon-tracking method for shipboard video stabilization and rectification.

In this paper we study how robust is the mean sea plane estimation when the plane orientation is determined using the 3-D data only (i.e. without complementary data sources for motion compensation), a condition that would greatly simplify the stereo processing. For the analysis reported in the study we have taken advantage of a Wave Acquisition Stereo System (WASS; Benetazzo, 2006) that was deployed onboard a vessel during a research cruise (Section 3.2). Preliminarily (Section 3.1), sea elevation data from a synthetic sea state have been used to asses to what extent the wave parameters (as the significant wave height) are well determined when a limited portion of the sea surface is retrieved by the stereo system. With reference to the wave spectral moments, this problem has already been investigated on time series and spatially distributed data by Krogstad et al. (1999). Section 2 of the paper reports the recent improvements of the WASS pipeline with respect to the layout described in Benetazzo et al. (2012). The developments proposed in this study allow getting more accurate and resolved 3-D data of the sea surface elevation. The study is completed (Section 4) with a detailed analysis of the possible uses of stereo systems mounted onboard research vessels and ships of opportunity.

2. The WASS observatory

WASS is an optical-based system used to collect space–time data of sea surface elevations. It relies upon a pair of high-resolution digital cameras, which, once synchronized, allow the sea waves to be observed from two distinct points of view.

With respect to the layout described in Benetazzo et al. (2012), WASS has been improved to ease the installation and calibration phases, which are critical to get accurate measurements. Such developments are described in the following sections.

2.1. Calibration: intrinsic parameters and recovery of the stereo camera pose

Intrinsic parameters of each camera composing the stereo system are calibrated using a hand crafted known target (i.e., a chessboard). Since we expect such target being generally affected by some imperfections (i.e. printing misalignments, small bumps or glitches) we implemented the method described in Albarelli et al. (2010) that suggest a bundle adjustment step to optimize both camera parameters and target geometry. Each camera is therefore calibrated independently by acquiring ~ 50 snapshots of the target with different orientations and distances from the camera, spanning a space about 3 m depth and 5 m wide in front of it. All the parameters are estimated by imposing zero skewness, square pixels, and a five coefficient polynomial radial distortion model.
The estimation of the intrinsic parameters is not enough to perform the stereo reconstruction from a pair of images. In fact, the reciprocal position of the two cameras (the so-called extrinsic parameters) must be provided to recover the full geometry of the scene through triangulation. The extrinsic parameters define the displacement $\boldsymbol{\tau}$ and the rotation R between the left and right camera frames according to the Euclidean transformation $g = (R, \boldsymbol{\tau})$. In previous WASS deployments, the rigid motion g was estimated by exposing an ad-hoc calibration target to both cameras, and by relating the known 3-D geometry of the target with its re-projection onto the image planes. However, even if this is the standard de-facto way to calibrate a stereo rig in laboratory conditions, this approach manifests several drawbacks when applied to stereo systems with large baseline.
At first, since for field applications we usually require a baseline $\boldsymbol{\tau}$ between cameras larger than 2 m, the target size has to be wider than 1×1 m^2, and placed at a distance greater than about 5 m from the cameras. Due to the target size, the manufacturing process may lead to some coarse imperfections and allowing the protrusion of such target meters away from the vessel hull can be time consuming or even dangerous. Moreover, the calibration procedure is time intensive and requires taking apart the device from its working position. As such, it is very difficult to modify the system geometry on-the-fly to accommodate different

acquisition requirements. For instance, it may be reasonable to take the device closer to the sea when the waves are slight, so a small but highly resolved sea surface region can be acquired. On the other hand, large waves demand a broader area, requiring the device to be repositioned farther from the surface. Finally, the "calibrate once and for all" strategy is not reliable since vibrations of the support and environmental factors, as wind, can modify the relative angle between cameras and jeopardize the reconstruction accuracy.

To overcome these limitations, we developed a calibration procedure that relies on the photometric consistency of the sea surface itself, and thus can be carried out during the acquisition without the need of a calibration target. Specifically, it is well known that it is possible to estimate the relative pose of two cameras, up to scale, from a set of corresponding points between the two images (Fig. 1).

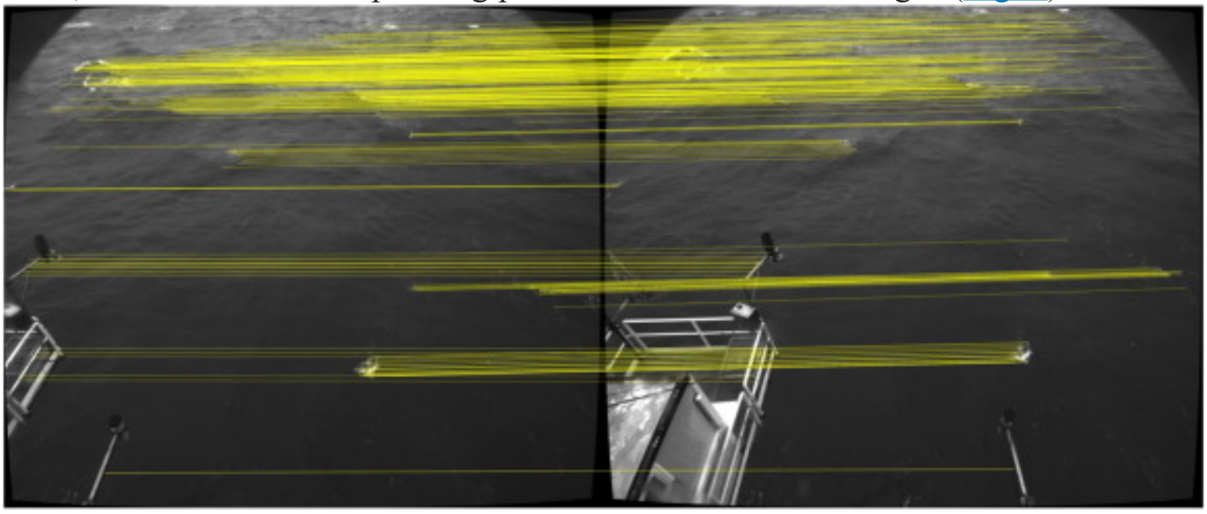

Fig. 1. Estimation of the stereo camera pose: example of the corresponding features in the two stereo-camera images. In the left and right images the corresponding pixels are connected with a yellow line. Stereo images are taken by a WASS mounted on the "Acqua Alta" oceanographic platform (northern Adriatic Sea, Italy).

Therefore, taking some points (in homogeneous coordinates) $p_1 \dots p_n$ extracted from a frame captured by the first camera (say left), and the corresponding set $p_1' \dots p_n'$ by the second (say right), the epipolar constraint can be exploited to estimate the essential matrix M such that (Ma et al., 2004)(1)$p_i M p_i' = 0, \forall i = 1 \dots n$. Moreover, the essential matrix can be decomposed through singular value decomposition to recover the rigid motion g up to a scale factor for $\boldsymbol{\tau}$ (Hartley and Zisserman, 2004). While conceptually simple, determining such corresponding points can be a difficult task particularly when dealing with un-textured areas or repetitive patterns. Not surprisingly, sea surface is not rich of distinctive features so special care has to be taken to let this process be as reliable as possible. In the stereo pipeline, the extrinsic calibration process starts with the extraction of a set of Speeded Up Robust Features (SURF; Bay et al., 2008) from each image. The algorithm is set to use 3 octaves, 8 intervals per octave and a blob response threshold of 10^{-4}. To obtain a more uniform spatial distribution of interest points in a frame, the image is divided in 16 blocks and points with lower hessian response are iteratively removed from each block to finally collect a set of 2600 features for each image. From these feature points, orientation, scale and a 64-component descriptor are computed.

Since most of these points are located on high textured areas (waves crest and white capped areas), the descriptor itself is not sufficient to establish a reliable set of matches between left and right camera features. Indeed, the local information around each point is not distinctive when dealing with a surface that shows uniform color, smooth shading, and clear but repetitive white areas. To guarantee a good set of point-to-point correspondences, we implemented the state-of-the-art method proposed in Albarelli et al. (2012). The key idea is that, for small motions, the transformation between stereo images that affects a group of close-by features can be approximated to be affine. Therefore, scale and orientation of each interest point may be used to define the similarity between two possible candidate matches as a function of their coherence with respect to the same affine transformation. To filter consistent sets of matches that are all mutually compatible, a non-cooperative evolutionary game is repeated many times to extract up to 30 groups with more than 5 matches each. After the inlier selection, most of the filtered correspondences are correct. We are able to obtain an average of 150 matches for each couple of left–right frames. To make the process even more robust, we embedded the subsequent essential matrix estimation step inside a RANSAC (random sample consensus) scheme to guarantee that the computed matrix is coherent with a large enough set of features. Specifically, we start by merging together all matches extracted from a sequence of *n* consecutive frames. From this set of matches, we iteratively extract 5 random elements and estimate all possible essential matrices (in general, with only five points there are many different solutions) by using the method presented in Nister (2004). These essential matrices are used to count how many points have its relative match nearer than one pixel from the corresponding epipolar line. After 50,000 iterations, the essential matrix coherent

with the largest number of matches is kept, and used to recover rotation and translation.
Due to the low rank of the essential matrix, the motion is recovered up to scale, i.e. the magnitude of the translation vector $\boldsymbol{\tau}$ is arbitrary. Since for wave measurements it's crucial to provide reconstructions with the correct scale, we estimate such parameter by showing a known object to both cameras. Despite being conceptually similar to the use of a calibration target, the estimation of the scale parameter alone is a very well-conditioned problem and thus it does not require a complex reference object. Indeed, we use an object of known shape that is captured for several consecutive frames. The ratio between the reconstructed 3-D object and its known dimensions gives the scale factor that has to be applied to the vector $\boldsymbol{\tau}$ to fix the baseline. Even if this estimation can be done just with a single stereo shot, we averaged the scale computed for a set of multiple frames weighted by the area of the object projection on each image. This leads to a more robust estimation.

2.2. Dense 3-D reconstruction

With the device calibrated, each image pair is stereo rectified and processed by a modified version of the dense stereo algorithm proposed by Hirschmüller (2008) available in the OpenCV library (Bradski & Kaehler, 2008; http://opencv.org), in order to match (with sub-pixel accuracy) all the pixels of the two stereo images (Fig. 2). The semi-global nature of the approach has the great advantage that it can relate the photometric consistency of several matching pixels to improve the reliability of the disparity map, especially for areas with loosely distinctive features. As a consequence, we can keep a relatively small window size (13 × 13 pixels) while still obtaining a precise localization of the matches. This corrects the matching bias in points around white-capped areas (Leckler et al. 2015) without introducing brightness equalizations or articulated pyramidal search approaches.

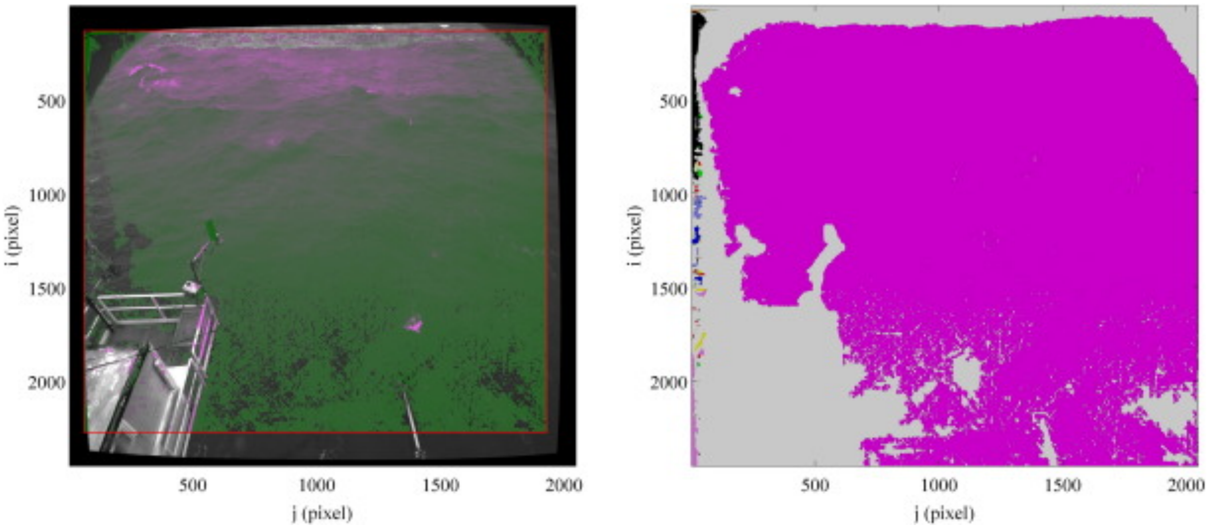

Fig. 2. Dense stereo reconstruction: example of disparity coverage (left panel) and graph component (right panel) in the right image plane. On the right panel, the biggest connected component of the graph is shown as purple region. Stereo images are taken by a WASS mounted on the "Acqua Alta" oceanographic platform (northern Adriatic Sea, Italy).

After the dense stereo process, a 3-D scattered point cloud is obtained for each frame pair. Even if the algorithm already filters the disparity map to reduce the noise of the produced output, its effectiveness is limited, as it cannot make assumptions on the reconstructed scene. Conversely, we expect the sea surface to be continuous and smooth everywhere. To greatly reduce the number of point outliers we use an additional filtering step taking advantage of the surface smoothness along the camera optical z-axis. We start by building a graph (Fig. 2) with the vertices being the reconstructed points and edges connecting each vertex with its 4-neighbors considering the adjacency relation of points induced by the image topology. For each edge, a weight is computed as the absolute difference of the z-components of their respective points coordinates. Then, each edge whose weight is greater than the 98th percentile of the weight distribution is pruned by the graph. The idea is to disconnect all the vertices exhibiting abrupt changes along the z-axis with respect to the neighbors. Finally, we filter out all the 3-D points not belonging to the biggest connected component of the graph.

2.3. 3-D mapping on the horizontal mean sea plane

Once the stereo method is applied to a stereo-pair image, the 3-D points have coordinates $\boldsymbol{X}_c = [x_c, y_c, z_c]^T$ referenced to the *camera* axes (Fig. 3), which are in general angled and displaced with respect to the horizontal mean sea plane (Fig. 3) Π_s: $a_s x_c + b_s y_c + c_s z_c + d_s = 0$.

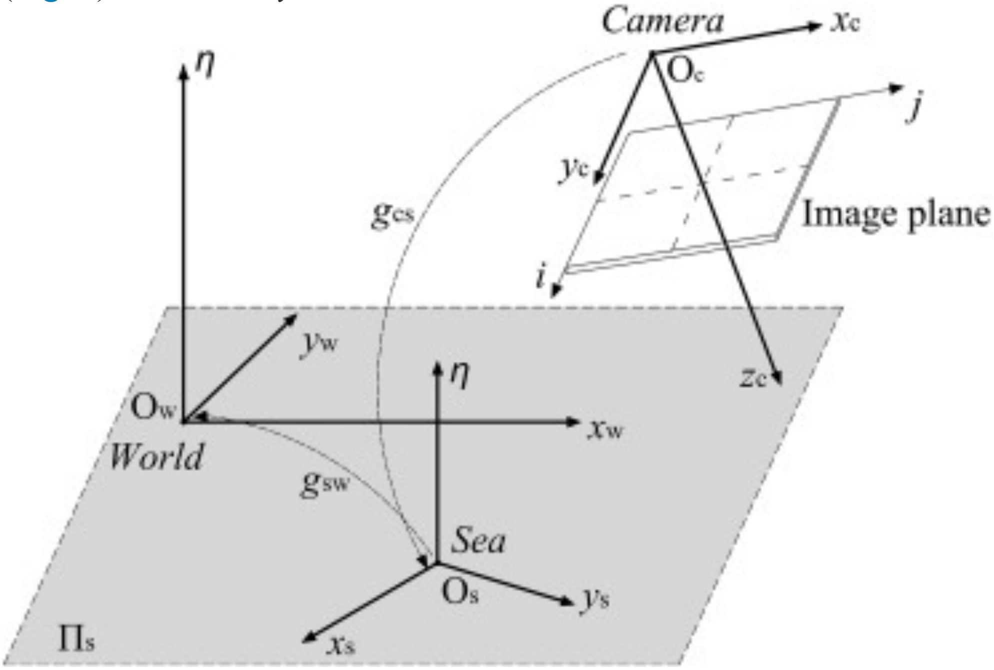

Fig. 3. Relative motion between the *camera* reference system (x_c, y_c, z_c), the *sea* reference system (x_s, y_s, η), and the *world* reference system (x_w, y_w, η). The horizontal mean sea plane Π_s is sketched as gray region.

For the purpose of wave observation, therefore, stereo data must be rotated (by a rotation matrix R_{cs}) and translated (by a translation vector $\boldsymbol{\tau}_{cs}$) to fulfill the required conditions that the x- and y-axis lie on Π_s, and the z-axis is vertically oriented and pointing upward (*sea* reference system, Fig. 3). Then, applying the *camera*-to-*sea* transformation $g_{cs} = (R_{cs}, \boldsymbol{\tau}_{cs})$ we obtain the 3-D vector(2)Xs=xsysηT=RcsXc+τcswhere η is the sea surface elevation that g_{cs} guarantees being measured orthogonally from the horizontal plane Π_s. Applied to the entire time (t) sequence of 3-D points the coordinate transformation (2) determines a space–time ensemble of sea surface elevations, viz. $\eta = \eta(x_s, y_s, t)$. We note that any transformation that transforms the sea plane in itself (i.e. a rotation around any axis parallel to the vertical axis) is not constrained by Eq. (2). Therefore an additional roto-translation (*sea*-to-*world* transformation) $g_{sw} = (R_{sw}, \boldsymbol{\tau}_{sw})$ must be accounted for to map the wave data onto the geographic coordinates (*world* reference system, Fig. 3), such that the positive y-axis is northward and the positive x-axis eastward, while vertical distances are kept unchanged according to(3)Xw=xwywηT=RswXs+τsw.

Whereas external sensors (a positioning system and a compass with sufficient accuracies) may provide parameters of the transformation g_{sw}, the estimation of g_{cs} is crucial to use WASS as a wave observatory system. The elements R_{cs} and $\boldsymbol{\tau}_{cs}$ are usually estimated by a linear least squares fitting of the 3-D data $\boldsymbol{X}_c$ in the *camera* reference system to get an approximation Π: $ax_c + by_c + cz_c + d = 0$ of Π_s. In the fitting procedure, 3-D data are weighted by the point distance with respect to the camera center. This partially compensates the non-uniform spatial density of the 3-D points due to the projective distortion of the sea plane caused by the angled cameras. As the area spanned by WASS is generally limited to few wave and crest lengths it is not a-priori ensured that at a given instant the Π-plane fits the mean sea plane Π_s; this implies, for instance, that coefficients $[a, b, c, d]$ are function of time and different from $[a_s, b_s, c_s, d_s]$.

In a fixed platform scenario, Π should not change over time. Thus, we can assume the estimation of its parameters being affected by zero-mean Gaussian random noise that can be effectively removed simply by time averaging. This has been proven (Benetazzo et al., 2012) to remove the influence of longer wave components that bias Π. The Π_s-plane coefficients are therefore given by

$$\Pi_s \approx E\{\Pi_t\} \rightarrow a_s \approx E\{a_t\};\ b_s \approx E\{b_t\};\ c_s \approx E\{c_t\};\ d_s \approx E\{d_t\} \tag{4}$$

where E{} denotes expectation. The rigid motion (2) is finally expressed as (Benetazzo, 2006)

$$R_{cs} = \begin{bmatrix} 1-\frac{(1-c_s)a_s^2}{a_s^2+b_s^2} & -\frac{(1-c_s)a_s b_s}{a_s^2+b_s^2} & -a_s \\ -\frac{(1-c_s)a_s b_s}{a_s^2+b_s^2} & 1-\frac{(1-c_s)b_s^2}{a_s^2+b_s^2} & -b_s \\ a_s & b_s & c_s \end{bmatrix} \tag{5}$$

$$\boldsymbol{\tau}_{cs} = [0, 0, d_s]^T. \tag{6}$$

On a moving vessel, the Π-plane coefficients cannot be averaged over the time sequence, as the stereo rig is continuously changing in time its position with respect to Π_s: Π-plane coefficients are hence also affected by the vessel motion. In this case, therefore, a different strategy must be adopted to correctly map the 3-D data onto the *sea* reference system. In this respect, the transformation (2) will be discussed in the following sections using a synthetic sea state, and realistic wave data collected by a WASS mounted on a vessel.

3. Assessment of the *camera*-to-*sea* transformation

3.1. Simulated sea waves

To asses the validity of the *camera*-to-*sea* transformation (2) applied to the instantaneous (at time t_i) 3-D wave field $z_c(x_c, y_c; t_i)$ we have firstly analyzed a

synthetic sea state. We have also assumed an ideal stereo system with down-looking cameras, i.e. the cameras *z*-axis is vertically oriented, the *xy*-plane is parallel to the horizontal plane, and the elevation $\eta = z_c$. Coefficients of the Π_s-plane are therefore known a priori and equal to $[a_s, b_s, c_s, d_s] = [0, 0, 1, 0]$, in a way that $\boldsymbol{X}_s = \boldsymbol{X}_c$; on the contrary, the unknown *Π*-plane coefficients $[a, b, c, d]$ are determined by fitting the 3-D data $z_c(x_c, y_c; t_i)$, as described in Section 2.3. This analysis is aimed at assessing the dependence of *Π*-plane and wave parameters upon the average number of spatial (i.e., 2-D) waves included within the stereo-camera field of view (FOV). We should expect that the more the waves are numerous, the better the mean sea surface orientation and position will be estimated, and, consequently, the wave data. In fact, up to now the sea surface area covered by WASS has been in the order of $100 \times 100\ m^2$, therefore few waves have been gathered on average by the stereo system. It is thus required to verify to what extent the *Π*-plane approximating Π_s is reliable to correctly map sea surface elevations from the *camera* onto the *sea* reference system.
The synthetic sea surface elevation field was obtained by simulating an evolving random sea surface $\eta(x, y, t) = \eta(x_s, y_s, t)$. To this end, we employed the WAFO toolbox for MATLAB® (WAFO Group, 2011; http://www.maths.lth.se/matstat/wafo/), which has been extensively applied for simulations of random seas (e.g. Gemmrich and Garrett, 2008). Without loss of generality, the simulation of a random sea is based upon the random-phase/amplitude model (Pierson et al., 1955), which assumes that a Gaussian sea surface is result of the summation of independent harmonic components of amplitude *b*, angular frequency *ω*, direction *θ*, and phase angle *Ψ*:(7)ηxyt=∑i=1N∑j=1Mbi,jcoskixcosθj+kiysinθj−ωit+Ψi,jwhere $\boldsymbol{k} = (k_x, k_y) = (k\cos\theta, k\sin\theta)$ is the wavenumber vector associated to the frequency *ω* (using the linear dispersion relationship for deep-water waves) and direction *θ*. Since the numerical simulation may be a highly computational demanding task, the space–time wave field $\eta(x, y, t)$ was computed in the Fourier space. Frequencies and directions were chosen for a proper representation of the sea surface elevation field, phase angles were randomly assigned from a uniform distribution in the range (0, 2π], and amplitudes were prescribed from a chosen directional wave spectrum $S(f, \theta)$. In order to simulate a random Gaussian sea surface using a finite number of components (namely *NM*), amplitudes must be chosen randomly (Tucker et al., 1984), generated from a Rayleigh distribution (Longuet-Higgins, 1952) with root

mean square value of $2Sf\theta\Delta f\Delta\theta$, where Δf and $\Delta\theta$ are the frequency and direction interval, respectively. In this study the wave spectrum $S(f, \theta)$ was derived combining a JONSWAP frequency spectrum (with spectral significant wave height H_{m0} = 1.04 m, peak frequency f_p = 0.22 Hz, and peak enhancement factor γ = 3.3; Hasselmann et al., 1973) with a $\cos^2\theta$ directional distribution function (Holthuijsen, 2008). The wave field was represented using spatial resolutions $\Delta x = \Delta y$ = 0.5 m, and temporal resolution Δt = 0.25 s; moreover, the sea state spanned a surface area of 140 × 250 m^2, and a duration of 900 s. The frequency–direction domain was discretized using 7200 equally-spaced frequencies ranging from 2.8 × 10^{-4} Hz to 2.00 Hz, and 180 equally spaced directions with 2° resolution. The x-axis of the sea state was selected coincident with the mean direction of wave propagation.

The spatial parameters of the sea state have been computed from the moments m_{pqr} of the frequency–direction wave spectrum given by(8)$m_{pqr}=\iint k_x^p k_y^q f^r S f\theta\, df\, d\theta$such that, in particular, the mean zero-crossing wave and crest lengths (L_x and L_y, respectively) are expressed as (Baxevani and Rychlik, 2006)(9)$L_x=2\pi m_{000} m_{200}, L_y=2\pi m_{000} m_{020}$which are L_x = 14.0 m and L_y = 24.2 m in the specific case of the wave spectrum studied here. The standard deviation of the space–time sea surface elevation field $\eta(x, y, t)$ is 0.26 m.

For the purpose of the present analysis, we have isolated on the xy-plane (Fig. 4) five different rectangular sea surface regions (labeled as A_j), whose sides are scaled according to L_x and L_y, such that region areas are given by(10)$A_j=jL_x jL_y=j^2 L_x L_y$with coefficients j = 1, 2, 4, 8, and 10. This implies, for example, that A_{10} encompasses on average 100 spatial waves at each time.

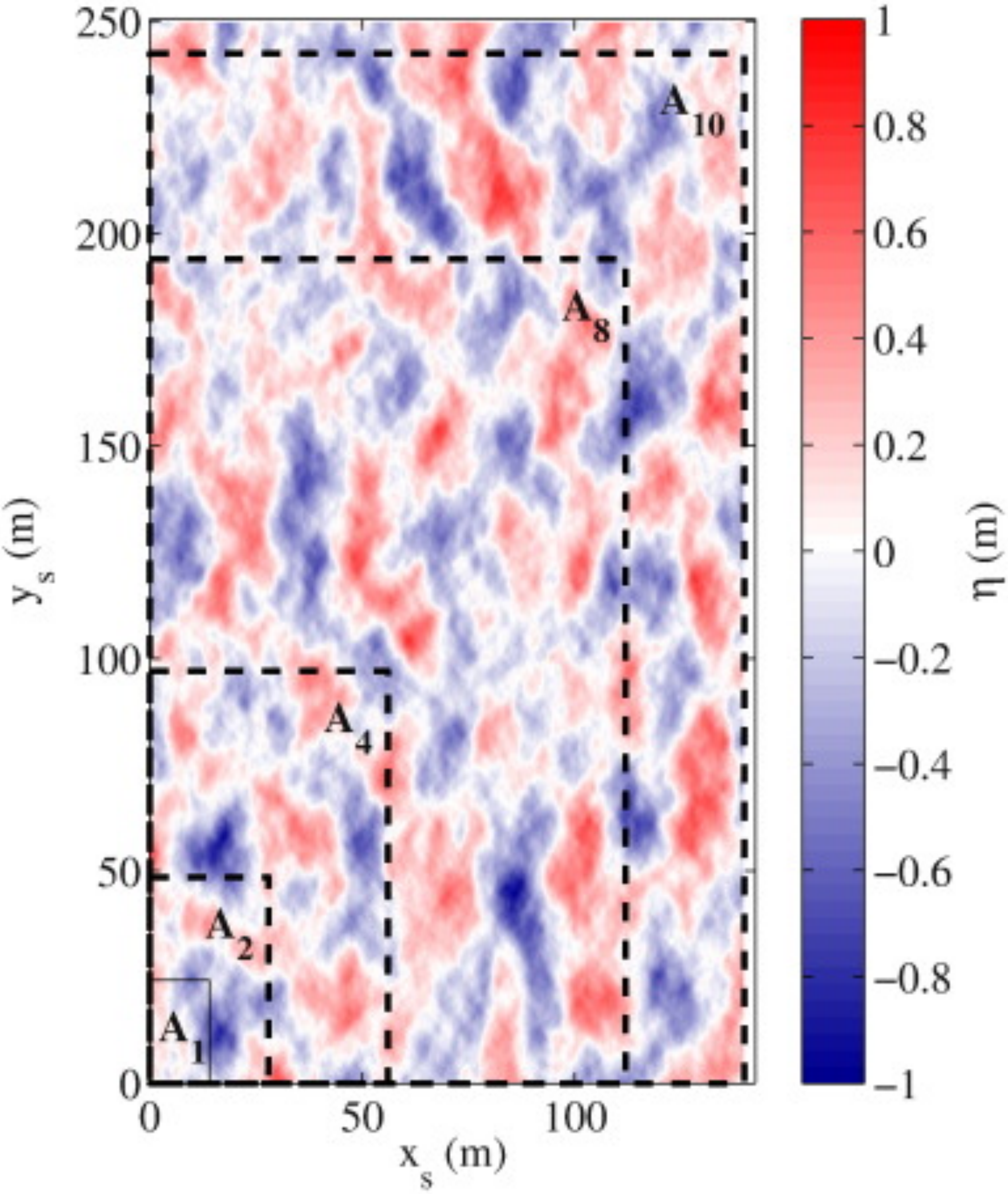

Fig. 4. Example of Gaussian 3-D wave field. Sea surface regions with different areas are bounded by black dashed lines and labeled as A_j (with j = 1, 2, 4, 8, and 10).

3.1.1. Influence on wave parameters of the sea surface area

The statistics of the instantaneous (at time t_i) simulated 3-D wave field bounded by the regions A_j, viz.(11)$\eta_{ji}:=\eta_{xy\in A_j;t=t_i}$is firstly derived (and shown in Table 1) to assess for each A_j the temporal variability of the mean value $E\{\eta_{ji}\}$ and standard deviation σ of the wave field η_{ji}. Over the time sequence of wave fields, the mean sea surface elevation (that should be zero by definition) experiences continuous variations, which are larger than about 0.17 m (about 16% of H_{m0}) for regions with area smaller than or equal to $4L_xL_y$ (A_2), and equal to 0.04 m (about 4% of H_{m0}) at most for the region A_4 (that encompasses 16 waves on average). Standard deviations of $E\{\eta_{ji}\}$ range for all areas between one-third and one-half of the maximal variations. At time t_i the statistical significant wave height of each subset η_{ji} is defined as four times the standard deviation as

$$H_s := 4\sigma = 4\left(E\{\eta_{ji}^2\} - E\{\eta_{ji}\}^2\right)^{1/2} \quad (12)$$

which is on average a fair approximation of H_{m0} for areas larger than or equal to $4L_xL_y$ (A_2). However, large variations of H_s have been observed over the time sequence for all regions, and not even the largest region (A_{10}) captures the severity of the sea state at each instant (indeed for A_{10} the standard deviation of H_s estimate is 0.05 m).

Table 1. Temporal variability of the sea surface elevation field within the subset regions A_j (with j = 1, 2, 4, 8, and 10). Maximum (Max), minimum (Min), average (Avg), and standard deviation (Std) of the mean elevation $E\{\eta_{ji}\}$ and the significant wave height $H_s = 4\sigma$.

Variable		$A_1 = L_xL_y$	$A_2 = 2^2L_xL_y$	$A_4 = 4^2L_xL_y$	$A_8 = 8^2L_xL_y$	$A_{10} = 10^2L_xL_y$
$E\{\eta_{ji}\}$ (m)	Max	0.46	0.16	0.04	0.02	0.01
	Min	− 0.49	− 0.17	− 0.04	− 0.02	− 0.01
	Avg	0.00	0.00	0.00	0.00	0.00
	Std	0.15	0.05	0.02	0.01	0.00
H_s (m)	Max	2.07	1.60	1.39	1.22	1.21
	Min	0.41	0.60	0.84	0.89	0.96
	Avg	0.89	1.04	1.04	1.04	1.04
	Std	0.25	0.18	0.11	0.07	0.05

In this respect, Krogstad et al. (1999) investigated the accuracy for estimates of wave spectral parameters, and their dependence on the sampling variability and the degrees of freedom of the spectrum. Importance of such an analysis is for example when comparing wave spectra from two different instruments. For 3-D wave fields, Krogstad et al. (1999) showed that the accuracy for estimate of the spectral significant wave height $H_{m0} = 4\ m_0$ (where m_0 is the zeroth-order moment of the wave spectrum) is an inverse function of the area A used to record the sea surface elevation. The relative error (called coefficient of variation, COV) in estimating H_{m0} is expressed as

$$COV = \frac{Std\{H_{m0}\}}{H_{m0}} = \frac{\sqrt{Var\{H_{m0}\}}}{H_{m0}} = \frac{4\sqrt{Var\{m_0\}/m_0}}{4\sqrt{m_0}} = \frac{\sqrt{Var\{m_0\}}}{2m_0} \quad (13)$$

where Std is the standard deviation for estimate and Var its variance. If we retain the instantaneous 3-D wave field to derive the spectral parameters the variance of m_0 is given by

$$Var\{m_0\} = \frac{4\pi^2}{A}\int S^2(k_x,k_y)\,dk_x\,dk_y \quad (14)$$

where $S(k_x, k_y)$ is the 2-D wave spectrum function of the wavenumber vector. Using the regions A_j and the spectrum adopted to generate the synthetic sea state COV assumes the values: $COV(A_1) = 0.52$, $COV(A_2) = 0.26$, $COV(A_4) = 0.13$, $COV(A_8) = 0.07$, and $COV(A_{10}) = 0.05$. For the smallest regions, COV is larger than the variability (Std) of H_s reported in Table 1, where the variations of wave parameters have been derived assuming that each 3-D wave field is properly descriptive of the sea state. On the contrary, regions A_4, A_8, and A_{10} have COV values close to the results in Table 1, most likely because these regions encompass a portion of the sea surface large enough to represent the actual randomness of the sea elevation field.

3.1.2. Influence on Π-plane coefficients of the sea surface area

As a consequence of the results shown in Section 3.1.1 large variations in estimates of wave parameters are expected for sea surface regions with small area relative to average lengths of waves. We should consequently expect changes of Π-plane coefficients over time, with the result that the fitting process provides a weak approximation of the mean sea plane Π_s. In fact, as the Π-plane coefficients result from a least-square operation than minimizes the variance of the data, it should be expected (as clearly visible in Fig. 5) that sea surface regions that bound a larger number of waves would provide a much more robust estimate of Π_s.

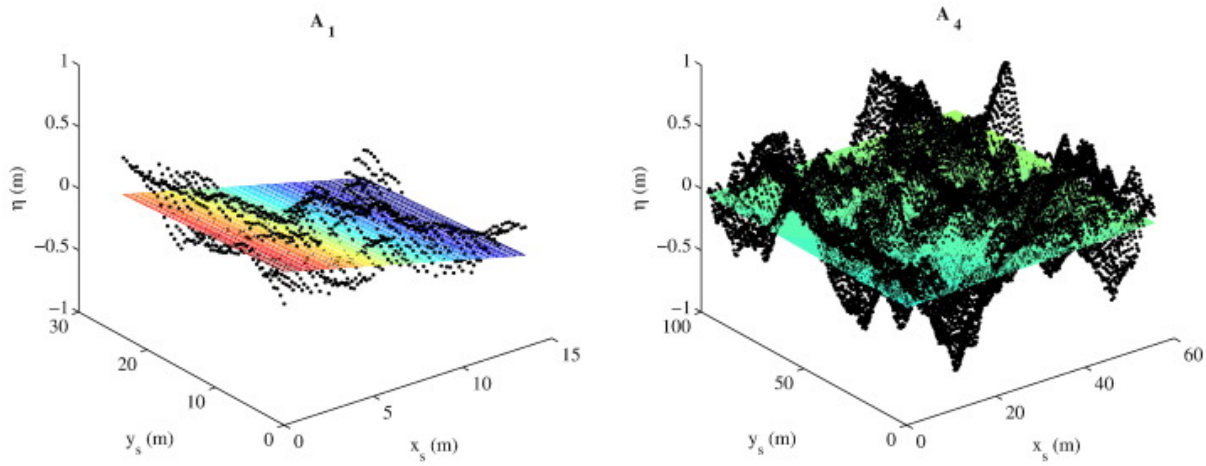

Fig. 5. Instantaneous sea surface elevation field (black dots) within two different regions A_j: example for regions A_1 (left panel) and A_4 (right panel). For each subset, the Π-plane fitting the 3-D field is also displayed as color mesh. The mean sea plane Π_s (not shown) is given by the surface $\eta = 0$.

In order to verify this, we have fitted a plane through the sea surface elevation field η_{ji} to obtain the plane Π: $ax_c + by_c + cz_c + d = 0$, and an approximation $\underline{X}_s(t_i) = \underline{R}_{cs}X_c(t_i) + \underline{\tau}_{cs}$ of the actual 3-D wave field $X_s(t_i) = \eta(x_s, y_s; t_i)$. We have expressed the Π-plane orientation in terms of the dihedral angles α_x and α_y between Π and the planes $x_s = 0$ and $y_s = 0$, which are given, respectively, by(15)αx=aa2+b2+c2αy=ba2+b2+c2.

Table 2 shows the statistics of the dihedral angles which are continuously changing with time; for example, variations larger than 0.3° are estimated for surface areas smaller than or equal to A_4. Additionally, the distance D of Π from the origin of the axes is expressed as(16)D=da2+b2+c2and it is also shows an evolution over the sequence of the wave fields (Table 2); for instance, for the region A_4, variations of D are smaller than about 20% the significant wave height. It is worth of noting that the time-average dihedral angles and distances shown in Table 2 correspond, for all subsets A_j, to the values of Π_s: this important result confirms that the mean plane coefficients computed as in Eq. (4) provide, from a fixed platform, a reliable estimate of the mean sea surface pose.

Table 2. Temporal variability of dihedral angles (α_x, α_y) and distance from the origin (D) of the Π-planes for different subset regions A_j (with j = 1, 2, 4, 8, and 10). For reference, dihedral angles of Π_s are α_x = 90° and α_y = 90°.

Variable		$A_1 = L_xL_y$	$A_2 = 2^2L_xL_y$	$A_4 = 4^2L_xL_y$	$A_8 = 8^2L_xL_y$	$A_{10} = 10^2L_xL_y$
a_x (°)	Max	95.9	91.9	90.3	90.1	90.0
	Min	83.4	88.1	89.7	89.9	90.0
	Avg	90.0	90.0	90.0	90.0	90.0
a_y (°)	Max	92.3	90.5	90.1	90.0	90.0
	Min	87.6	89.5	89.9	90.0	90.0
	Avg	90.0	90.0	90.0	90.0	90.0
D (m)	Max	1.15	0.52	0.20	0.06	0.04
	Min	− 1.02	− 0.50	− 0.16	− 0.06	− 0.04
	Avg	0.00	0.00	0.00	0.00	0.00

To complete the analysis of the synthetic sea state, we have extracted from the simulated space–time field $\eta(x, y, t)$ at the position $[x, y] = [0, 0]$ the time series of sea elevations $\eta_0 := \eta_0(t) := \eta(0, 0; t)$. The wave record η_0 has been compared to the corresponding (η_{0j}) derived at the same location from the space–time fields determined rotating the 3-D data using the Π-plane coefficients computed for each η_{ji} datum. In doing this, we have therefore constructed five (j = 1, 2, 4, 8, and

10) new space–time ensembles of sea surface elevations whose 3-D coordinates depend somehow on the likelihood between Π and Π_s. The correlation coefficient (*CC*) and the root-mean square difference (*RMSD*) between η_0 and η_{0j} show (Table 3), again, that a relatively large number of waves have to be included within each 3-D wave field to ensure that the fitting procedure provides a robust mean sea plane estimation, and, consequently, reliable wave data.

Table 3. Comparison statistics between time series of sea surface elevations taken from the synthetic wave field and after its roto-translation according to the Π-plane coefficients. Results are shown for different subset regions A_j (with j = 1, 2, 4, 8, and 10).

Variable	$A_1 = L_xL_y$	$A_2 = 2^2L_xL_y$	$A_4 = 4^2L_xL_y$	$A_8 = 8^2L_xL_y$	$A_{10} = 10^2L_xL_y$
CC	0.37	0.83	0.98	1.00	1.00
***RMSD* (m)**	0.31	0.18	0.06	0.02	0.01

3.1.3. Discussion

Results presented in the two previous sections show that for stereo applications from a moving structure, at least about sixteen 2-D waves must be included within 3-D wave field to derive an estimate of the mean sea plane orientation with maximal errors smaller than 0.3°, and to compute H_s values with mean variability smaller than about ± 10%. In these conditions, however, large instantaneous variations of waves parameters have still been observed. Moreover, a proper approximation of the mean sea plane is far to be valid for small $Area/L_xL_y$ ratios, for which a different strategy (for example tracking the horizon within the images, as done for instance in the study of Brandt et al., 2010, or using external instruments that provide vessel's orientation and position) for the estimation of the Π_s-plane must be adopted.

It is worth noting that the fitting procedure of 3-D data in the *camera* reference minimizes the sea surface elevation variance, thus the standard deviation of wave fields mapped by Eq. (2) is smaller than or equal to actual value of the sea state, i.e. $\sigma[\underline{\mathbf{X}}_s(t_i)] \leq \sigma[\mathbf{X}_s(t_i)]$. The consequence is that the significant wave height is underestimated, to an amount inversely proportional to the relative spatial extension of the 3-D wave field. This underestimation has been here quantified by means of the time series of H_s computed using the simulated 3-D wave fields η_{ji} and their re-mapping according to the best-fitting Π-plane coefficients for each region A_j and instant t_i. The *RMSD*, normalized to H_{m0}, between the original and transformed series is equal to 29.8% for A_1; 11.2% for A_2; 1.2% for A_4; 0.1%

for A_8; and 0.1% for A_{10}. It could be therefore argued that for sea surface region larger than A_4 bias of H_{m0} is pretty small, while for the smallest regions the error becomes not negligible.
The synthetic waves have been also used to assess the influence of the sea surface region orientation. In this respect, regions A_j have been rotated of 90° (with respect to the layout shown in Fig. 4) and sea surface data analyzed as done in earlier sections. Results (not shown here) prove that statistical parameters reported in Table 1 and dihedral angles given in Table 2 are slightly (differences of few percent) affected by the orientation of the sea surface region only for the largest subsets (A_4, A_8, A_{10}). On the other hand, parameters of the wave fields bounded by the smaller regions (A_1, A_2) are largely influenced by the orientation of the subset, up to, for example, 22% of Max H_s (Table 1) for region A_1. Notwithstanding, the analysis on the rotated regions confirms that small variations of the instantaneous sea state parameters are attained only for regions that encompass on average a large (say at least about 16) number of waves.

3.2. Observed sea waves

3.2.1. WASS experiment on a moving vessel

We have argued that the rigid motion (2) that maps 3-D wave data from the *camera* to the *sea* reference system is well estimated on a fixed platform by the time-averaging procedure (4) that cancels the influence on Π-plane coefficients of instantaneous and local sea surface elevations. When the platform is moving, however, this averaging procedure is not feasible, and therefore each 3-D wave field $z_c(x_c, y_c; t_i)$ is roto-translated according to its own set of coefficients. The latter condition was faced when we deployed a WASS onboard the Research Vessel R/V "Urania" (managed by the Italian National Research Council, CNR) during a cruise conducted in April 2013 in the southern Adriatic Sea region (Fig. 6). The two WASS digital cameras were deployed on the captain deck about 10 m above the mean sea level, and firmly placed side-by-side (baseline was 2.5 m) looking toward the sea surface (Fig. 6). This WASS had a setup similar to that one used in previous installations (Benetazzo et al., 2012) and consisted of two 5-megapixel cameras (2048 columns by 2456 rows array of 3.45 μm square active elements) connected to an external trigger to ensure synchronous grabbing of images. Camera lenses (with focal length equal to 5.0 mm) were chosen such that the lens angular aberration was minimized. Stereo camera calibration and processing followed the pipeline described earlier in Section 2. WASS has also been synchronized to the ship-mounted Global Positioning System and Compass, but the data provided by the Compass only were used with the purpose of compensating the ship motion and aligning the 3-D wave fields $\eta(x_s, y_s; t_i)$ with the *world* reference system axes. Starting at 08:12 UTC on April 14, 2013, WASS recorded at 15 Hz a 12-minute long stereo-image sequence, resulting in 10,080 stereo pairs. The *camera* reference system was set such that the camera *x*-axis (i.e. pixel rows) was horizontal and approximately parallel to the vessel's surge axis (Fig. 6). During the WASS acquisition, the vessel head was maintained to wind, which onboard was measured blowing, on average, toward 132°N with mean wind speed (at 10-m height) U_{10} = 7.1 m/s. During the experiment the vessel experienced a drift with mean speed of 0.23 m/s, so that the vessel displacement during the acquisition was small (about 170 m), such that we can assume the wave field homogeneous during the experiment. At the geographical position of the stereo acquisition, the water depth (*d*) was about 1000 m, therefore sea surface waves were in deep water condition.

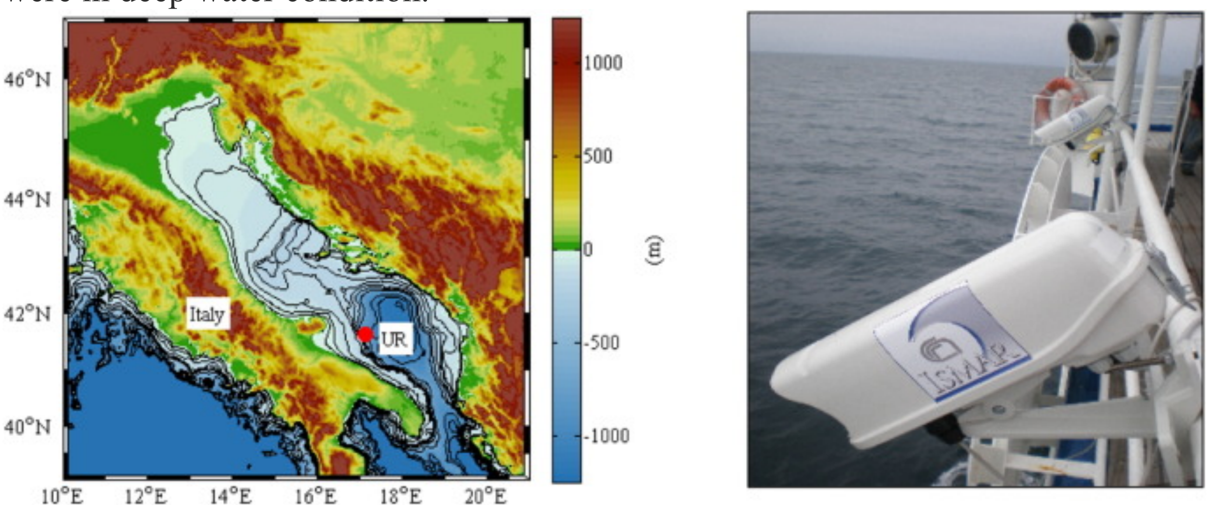

Fig. 6. Location (UR in the left panel) of the R/V "Urania" during WASS acquisition in the southern Adriatic Sea (Italy), and (right panel) installation of the stereo cameras on the handrail of the captain's deck.

Expected accuracy of the stereo observations have been derived using the formulations of the quantization error (Rodriguez and Aggarwal, 1990), which is function of the stereo-camera setup and position with respect to the mean sea plane (Benetazzo, 2006). We have also assumed that the sub-pixel stereo matching improves the accuracy by a factor of five, a conservative bound with respect to previous analyses (Benetazzo et al., 2012). For the stereo data collected onboard "Urania", the quantization error along the *z*-axis is displayed as 2-D map in Fig. 7. Root-mean-square (RMS) and absolute maximum (Max) errors along the *x*-, *y*-, and *z*-axis are $[RMS, Max]_x$ = [0.02 m, 0.10 m], $[RMS, Max]_y$ = [0.04 m, 0.16 m], and $[RMS, Max]_z$ = [0.01 m, 0.03 m].

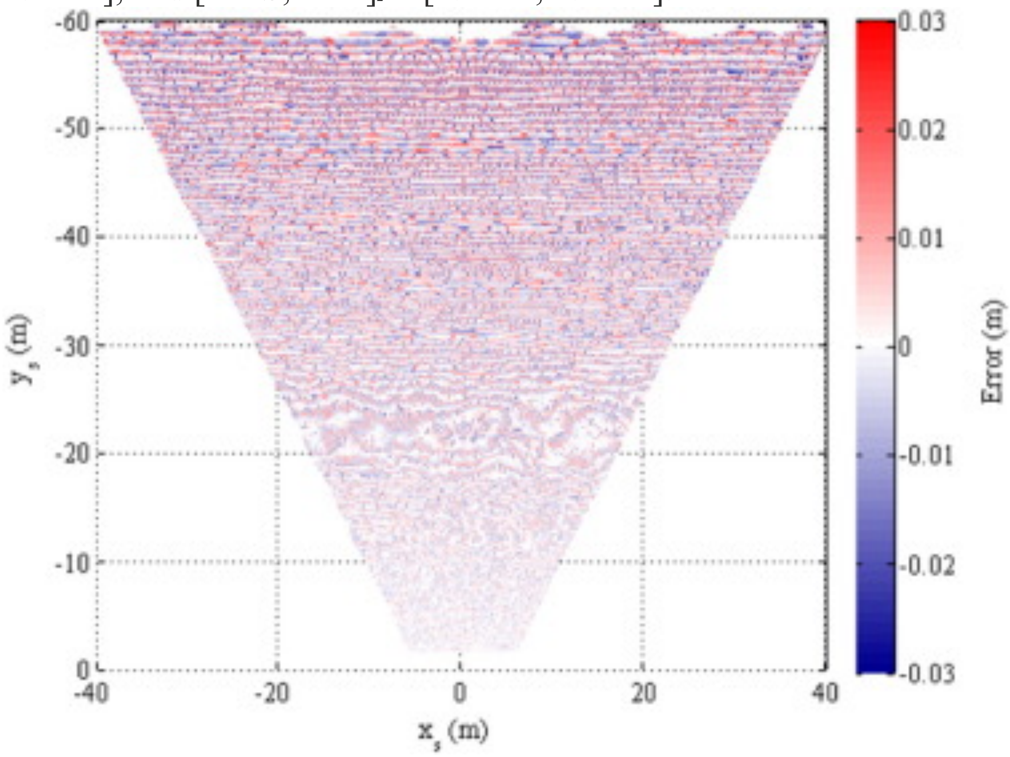

Fig. 7. Map of the quantization error for sea surface elevations (*z*-axis) within the stereo-camera field of view. Errors are displayed in the *sea* reference system.

As stated previously, because of the vessel motion, the *camera*-to-*sea* transformation was derived assuming suitable the approximation $\Pi = \Pi\,(t) \approx \Pi_s$ at each instant *t* of the stereo sequence. This should not be the case whether WASS would gather sea areas holding a limited number of waves, as discussed earlier in Section 3.1. Firstly we use the sea elevations data $\boldsymbol{X}_s$ and $\boldsymbol{X}_w$ to estimate some parameters of the sea state. In this respect, each 3-D data cloud $\boldsymbol{X}_c(t)$ was firstly transformed to $\boldsymbol{X}_s(t)$ according to the coefficients of $\Pi(t)$, and then aligned with the geographical axes to recover $\boldsymbol{X}_w(t)$. Scatter 3-D data were finally linearly interpolated on a spatial grid with uniform *xy*-resolution of 0.2 m (Fig. 8).

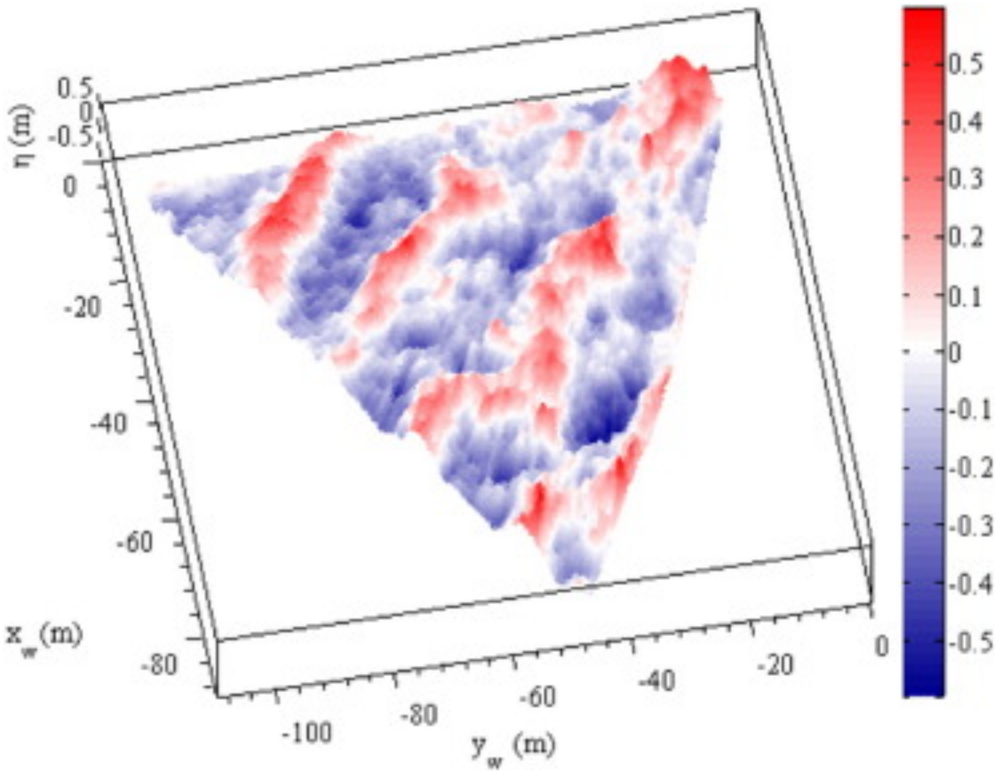

1. Download : Download high-res image (127KB)
2. Download : Download full-size image

Fig. 8. Examples of 3-D wave field in the *world* reference system. Only compass data are used to align 3-D axes with the *world* reference system.

3.2.2. Wave parameters

Once mapped on the *sea* reference system, the 3-D wave field at the instant t_i, viz. $\eta(x_s, y_s; t = t_i)$, has been used to estimate the wave energy spectrum in wavenumber coordinates, $S(\boldsymbol{k}) = S(k_x, k_y)$, using a 2-D Fourier transform. Specifically, we have selected a rectangular sea surface area of 39.0 m by 51.0 m, for which the spectral resolutions are 0.16 rad/m and 0.12 rad/m along the x_s- and y_s-axis, respectively, and the upper wavenumber limit is 15.7 rad/m along both axes. After the Fourier transform, spectral axes have been aligned with the *world* reference system (i.e. with y-axis pointing northward), and spectral energies averaged over the 12-minute long stereo sequence. Finally, the mean $S(\boldsymbol{k})$ spectrum has been transformed in polar coordinates to obtain the wavenumber–direction spectrum in accordance with the relation (Holthuijsen, 2008)(17)Skθ=Skxkykwhere θ is the direction of the vector $\boldsymbol{k}$. The $S(k, \theta)$ spectrum (Fig. 9) shows a unimodal sea state, with spectral significant wave height $H_{m0} = 4\, m_0 = 0.66$ m, mean direction of wave propagation $\theta_m = 116°$N, and peak direction of wave propagation $\theta_p = 110°$N. We note that using a 2-D Fourier transform the wavenumber-direction spectrum (17) is intrinsically biased by a 180°-ambiguity for wave directions. Thus, in this respect, Fig. 9 shows half of the actual $S(k, \theta)$ spectrum obtained using the wind direction data and assuming the peak direction of wave propagation as reference to partition on two halves the wave energy distribution. This ambiguity could be resolved only if the phase speed vectors were available for each wave component. On a fixed platform this is achievable (Gallego et al., 2011, Leckler et al., 2015) computing the 3-D spectrum $S(k_x, k_y, f)$, which is not derivable using stereo data collected from a moving structure. For the latter, different strategies must be adopted, for instance by means of cross spectral methods between consecutive stereo data (Jähne, 1993).

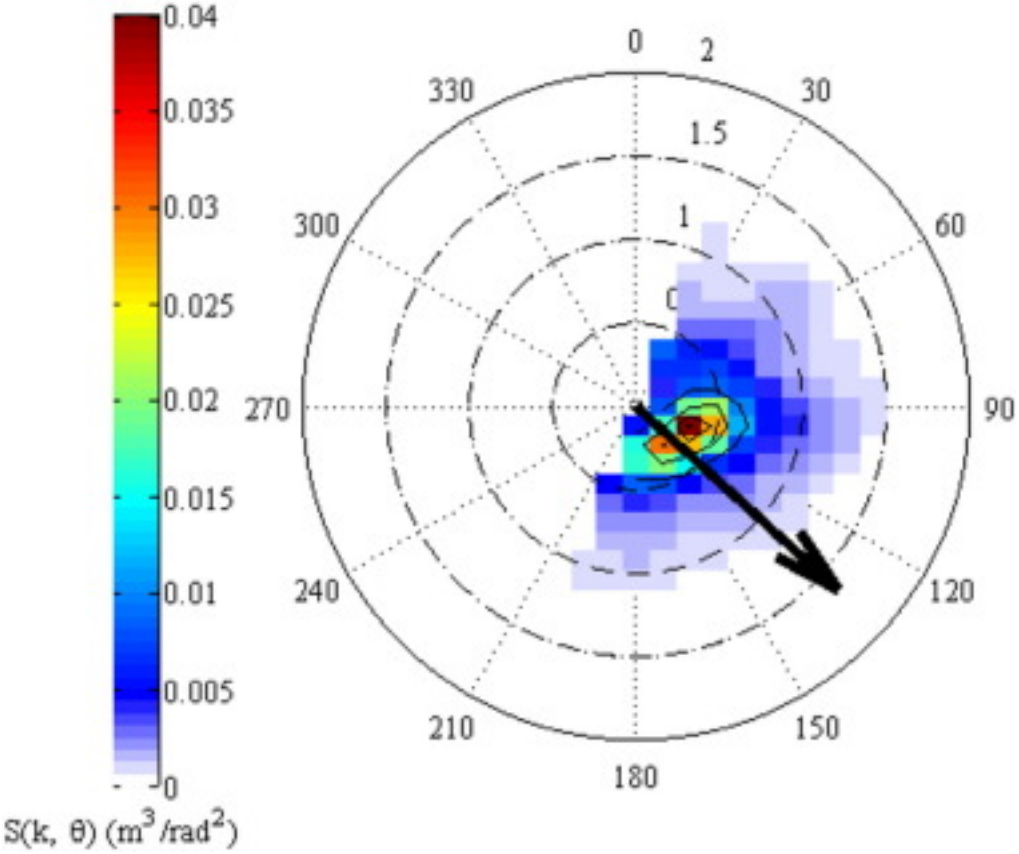

Fig. 9. Observed wavenumber–direction spectrum of the sea surface elevation field. The black arrow corresponds to the surface wind vector. The spectrum is plotted in the interval $[\theta_p - 90°, \theta_p + 90°]$, where θ_p is the peak direction of wave propagation. Directions of wave propagation are measured clockwise from north.

Spectral wave lengths have been computed from the directional spectrum applying an additional rotation to align the x-axis with the mean direction of wave propagation θ_m. The moments m_{pq} of the wavenumber–direction spectrum given by

$$m_{pq}=\int k_x^p k_y^q S(k,\theta-\theta_m)\,dk\,d\theta \tag{18}$$

have been therefore used to compute the mean wave (L_x) and crest (L_y) lengths as

$$L_x=2\pi\sqrt{\frac{m_{00}}{m_{20}}},\quad L_y=2\pi\sqrt{\frac{m_{00}}{m_{02}}} \tag{19}$$

For the stereo data collected onboard "Urania", these lengths are $L_x = 7.4$ m and $L_y = 10.3$ m. As the trapezoidal region of the sea surface spanned by the stereo data was approximately $A = 4000\ m^2$, i.e. about 53 times larger than the L_xL_y, WASS coverage resembles the subset A_8 of the synthetic sea state analyzed in Section 3.1. This suggests that the pose of the mean sea plane should be determined with a maximal orientation error in the order of 0.1°.

3.2.3. Sensitivity to the Π-plane orientation

During the cruise no data were available to provide the actual mean sea plane, so we have performed an a-posteriori assessment of the wave data mapped onto the *sea* reference system. To this end, to assess the sensitivity of wave data to the mean sea surface estimation, the Π-plane orientations (function of time) were modified by perturbing the dihedral angles by a uniform rotation $\Delta\alpha$ that was assumed taking the values [− 2.0°, − 1.0°, − 0.5°, − 0.1°, 0.0°, 0.1°, 0.5°, 1.0°, 2.0°]. Once biased, Π-plane coefficients have been used to re-map the 3-D fields $\boldsymbol{X}_c(t)$ onto $\boldsymbol{X}_s(t)$. Each $\Delta\alpha$, therefore, has produced a new space–time wave field $\eta = \eta(x_s, y_s, t)$, which has been characterized by the following quantities:

- Expected value of η: $E\{\eta\}$.
- Significant wave height H_s expressed as four times the standard deviation σ of η:

$$H_s=4\sigma \tag{20}$$

- Skewness coefficient of η:

$$\lambda_3=\frac{E\{(\eta-E\{\eta\})^3\}}{\sigma^3} \tag{21}$$

- Kurtosis coefficient of η:

$$\lambda_4=\frac{E\{(\eta-E\{\eta\})^4\}}{\sigma^4} \tag{22}$$

- Cross-Correlation coefficient (CC_G) between the empirical probability density function (pdf) of the dimensionless elevation $h = \eta / \sigma$ and the Gaussian pdf given by

$$p(h)=\frac{1}{\sqrt{2\pi}}\exp\left(-\frac{h^2}{2}\right) \tag{23}$$

•Cross-Correlation coefficient (CC_{GC}) between the empirical and the nonlinear pdf, which is approximated by a Gram–Charlier series including λ_3 and it is expressed as (Longuet-Higgins, 1963)

(24)ph=12πexp−h221+λ36h3−3h.

Results presented in Table 4 confirm that the *camera*-to-*sea* transformation is sensitive to the orientation of the mean plane. In particular, uncertainties in the estimation of the orientation larger than or equal to 2.0° produce negative skewness, while kurtosis coefficients close to 3 (typical of linear or weakly nonlinear sea waves) are associated to biases $-0.1° \le \Delta\alpha \le 0.1°$, which produced wave elevations distributed consistently ($CC_G \approx CC_{GC} \approx 1$) with the theoretical models (23), (24). Attention must be paid to the variance of the wave field. As for the synthetic sea state, the variance (and so the significant wave height) depends upon the mean sea plane orientation: while biases of ± 0.1° slightly affect H_s (differences of few %), the significant wave height is overestimated by assuming the orientation biased more than ± 0.5° (a variability typical of subset regions ranging between A_2 and A_4 of the synthetic sea state analyzed in Section 3.1).

Table 4. Effect on sea surface elevation statistics of perturbed *Π*-planes. Parameters corresponding to unbiased planes are shown for $\Delta\alpha = 0.0°$. The orientation bias of ± 0.1° is associated to the sea surface region spanned by the stereo camera FOV during the experiment onboard the R/V "Urania".

Δ*α* (°)	**2.0**	**1.0**	**0.5**	**0.1**	**0.0**	**− 0.1**	**− 0.5**	**− 1.0**	**− 2.0**
E{*η*} (m)	− 0.52	− 0.28	− 0.15	− 0.04	0.01	0.00	0.12	0.26	0.55
H_s (m)	2.24	1.30	0.89	0.70	0.68	0.69	0.87	1.30	2.40
λ_3	− 0.04	0.03	0.10	0.13	0.13	0.13	0.13	0.14	0.13
λ_4	2.02	2.37	2.81	3.05	3.06	3.05	2.87	2.41	2.03
CC_G	0.94	0.98	1.00	1.00	1.00	1.00	1.00	0.98	0.94
CC_{GC}	0.94	0.98	1.00	1.00	1.00	1.00	1.00	0.98	0.94

4. Use of stereo wave imaging in oceanographic studies

4.1. Collection of space–time wave data

Wave data are routinely collected by instrumentation (e.g., buoys) apt to gather the time evolution of the sea surface elevation at a fixed position of the sea. Such a local measurement has extensively been integrated with remote sensed data, from satellites, for instance, which retrieve spatially-distributed wave parameters along the flight track. In this context, wave fields collected from ships of opportunity would be beneficial given the availability of these facilities on the seas around the globe. Stereo wave imaging may be exploited for this purpose, because it merges the advantages of a remote observation with a high accuracy of the measurement.

In this respect, we have shown in Fig. 9 that an outcome of stereo wave data collected from a vessel is the directional distribution of wave energy over wavenumbers. The directional spectrum $S(k, \theta)$ integrated over direction, viz.

$$S(k)=\int_{-\pi}^{\pi} S(k,\theta)\,d\theta \quad (25)$$

provides the so-called omnidirectional wavenumber spectrum, which represents the directional sum of energy levels for a given wavenumber. The spectrum $S(k)$ has a rationale similar to that of the omnidirectional frequency spectrum $S(f)$; as a matter of fact, $S(k)$ and $S(f)$ are linked by the conversions (Holthuijsen, 2008)

$$S(k)=S(f)J_{fk} \qquad S(f)=S(k)J_{kf} \quad (26)$$

where $J_{fk} = df / dk$ and $J_{kf} = dk / df$ are the Jacobians used to transform the wave spectrum from the frequency to the wavenumber domain and vice versa. With regard to the experimental stereo data described in section 3.2, the omnidirectional wavenumber spectrum is depicted in Fig. 10: $S(k)$ shows a single energy peak followed by regions exhibiting power-law behavior approximately proportional to $k^{-5/2}$, a typical shape already outlined by theoretical analysis (Zakharov and Filonenko, 1967), numerical studies (Onorato et al., 2002), and observations (Hwang et al., 2000, Romero and Melville, 2010). The value of the saturation $S(k)k^3 \approx 0.01$ is close to those found by Banner et al. (1989) and Leckler et al. (2015) for young wind waves. The collection of saturation levels for different sea conditions (e.g., for wave fields with different steepness) is required for assessment of the wave breaking probabilities parameterization (Banner et al., 2000, Phillips, 1984), and their implementations into numerical wave models (Ardhuin et al., 2010). In this context, the stereo-image series collected by the cameras are also a unique source of data to detect and track breaking events on the sea surface (Mironov and Dulov, 2008), whose empirical probabilities can thus be compared with the aforementioned parameterizations (Leckler, 2013).

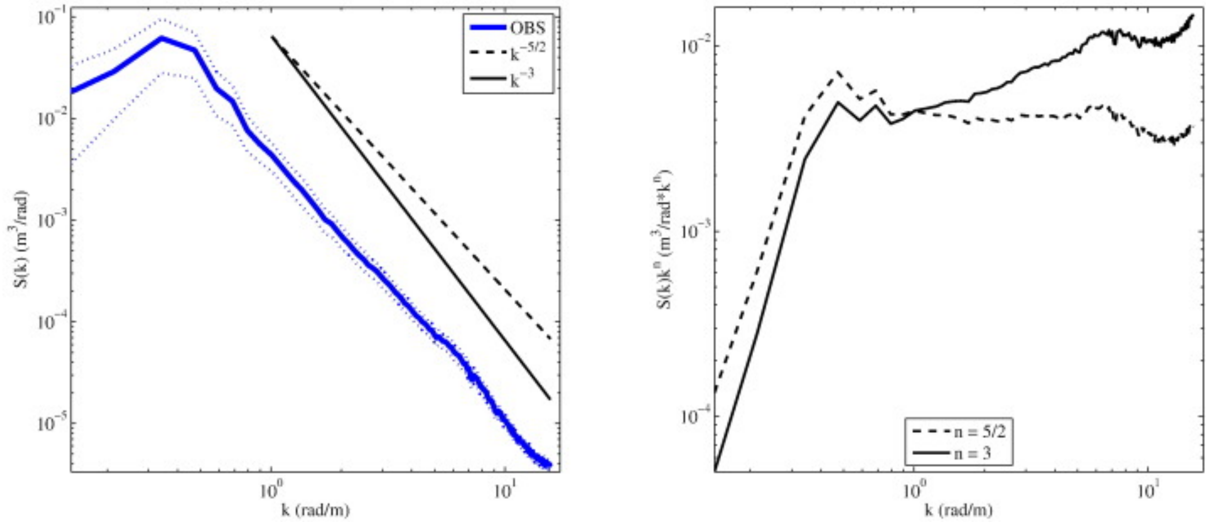

Fig. 10. (left panel) Observed omnidirectional wavenumber spectrum of the sea surface elevation field (continuous blue line) and associated stability band (dashed blue lines). The black dashed and solid lines are reference spectral slopes proportional to $k^{-5/2}$ and k^{-3}, respectively. (right panel) Wavenumber saturation spectra.

Besides the spectral properties, local wave information can be analyzed from a 2-D spatial perspective using the space–time wave field $\eta(x_w, y_w, t)$. For instance, the joint probability distribution function of wave heights H and periods T has been extensively studied using time records of the sea surface elevation (Cavanie et al., 1976, Longuet-Higgins, 1975, Shum and Melville, 1984), but very few studies (e.g. Romero and Melville, 2011, Xu et al., 2004) are available that analyzed the joint distribution of wave heights and wavelengths L. These wave characteristics can be computed at every time of the 3-D wave field sequence using a zero-crossing analysis along the peak direction of wave propagation. The resulting distribution of wavelengths and corresponding wave heights is shown in Fig. 11. The empirical wave slope H/L is equal to 0.03 on average and 0.09 at most, such that the Miche limiting steepness (Miche, 1944) expressed as(27) $H_{max}=\frac{2\pi}{7k}\tanh kd$ is not violated over the range of observed waves.

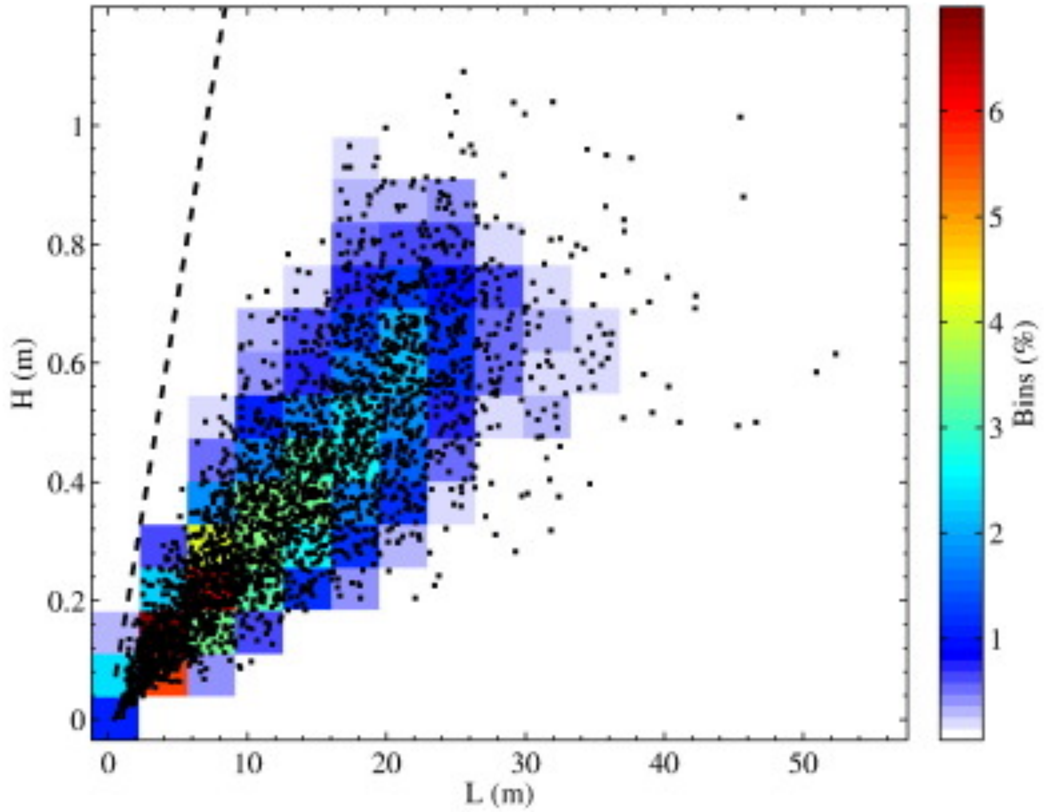

Fig. 11. Empirical wave height–wavelength joint probability function (black dots and color mesh). Theoretical Miche–Stokes upper bound is shown as dashed black line.

In addition, space–time wave data provide evidence of the 3-D wave groups' modulation. Results of Benetazzo et al. (2015) shown that one can grab these groups when they are close to the apex of their development and display large crest heights compared to the severity of the sea state (as shown for instance in Fig. 12). The extent of these crests (occasionally exceeding the threshold $1.25H_s$ used to define a single wave as “rogue” or “freak”) is well approximated by outcomes of a nonlinear space–time model (Benetazzo et al., 2015) derived from the predictions of extreme elevation probabilities in multidimensional random seas (Adler and Taylor, 2007, Fedele, 2012, Piterbarg, 1996). Space–time models predict wave extreme probabilities larger than those derived by the standard statistics relying, for instance, on time records of sea surface elevations (Benetazzo et al., 2015, Fedele et al., 2013). Nonetheless, space–time models have not been completely validated (e.g. Sclavo et al., 2015) under realistic different sea conditions (as theoretically investigated in Barbariol et al., 2015). A promising application of stereo systems onboard traveling vessels is therefore the potential contribution to refine and assess the application limits of space–time theories for wave extremes.

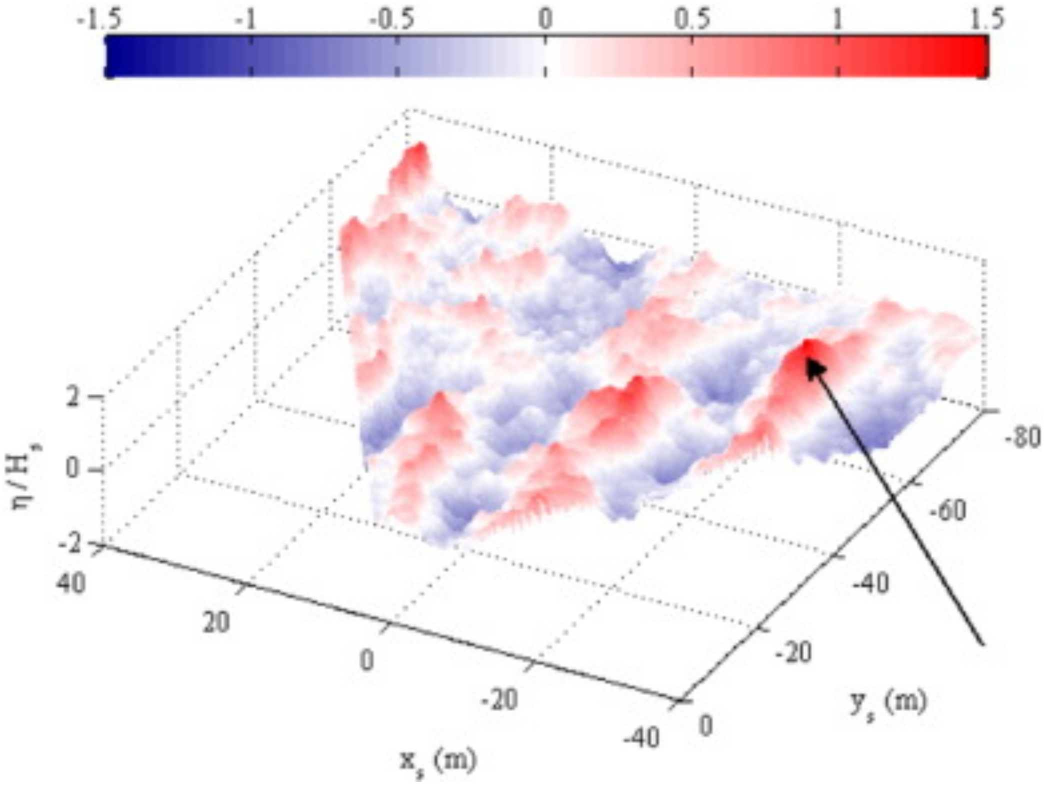

Fig. 12. Example of instantaneous dimensionless wave elevations η/H_s at a time when $\max\{\eta/H_s\} = 1.49 > 1.25$ (i.e. the common threshold used to call a wave a rogue wave). The wave crest where $\max\{\eta/H_s\}$ occurs is pointed by the black arrow.

4.2. Assessment of numerical wave models

Numerical wave models require observations to assess model parameters in hindcast and forecast studies. The variable integrated by this class of models is the variance density spectrum expressed as function of frequency and direction $S(f, \theta)$, or wavenumber and direction $S(k, \theta)$. As the directional spectrum $S(k, \theta)$ can be retrieved using stereo systems, they produce observatory data that can be integrated into numerical studies (for instance adopting assimilation techniques for the correction of wave fields). As a case test, we have implemented a numerical model to reproduce the wave conditions during the WASS experiment described in Section 3.2. In order to simulate the wave characteristics, the third-generation wave model simulating wave nearshore (SWAN; Booij et al., 1999) has been implemented. SWAN is a state-of-the-art spectral wave model, which computes short-crested wind-generated waves, accounting for generation, redistribution, and dissipation of the wave action density spectrum. The SWAN model solves a radiative time-dependent transport equation in the variable $S(f, \theta)$, assuming positive (wind input) and negative (dissipation terms in deep and shallow waters) source terms. In this study, the directional spectrum was discretized over an uniform grid of 6.0 × 6.0 km^2 covering the portion of the Mediterranean Sea between 1–21°E and 33–46°N. The wave spectrum was resolved with 40 intrinsic wave frequencies geometrically distributed, such that $f_{n+1} = 1.1 f_n$, with $f_1 = 0.05$ Hz and $f_{40} = 2.00$ Hz, and 36 equally spaced directions covering the full circle. Wind forcings were provided by high-resolution (i.e., 7.0 × 7.0 km^2) fields computed by COSMO-I7 (Russo et al., 2013), the Italian version of the COSMO Model, a mesoscale model developed in the framework of the COSMO Consortium (http://www.cosmo-model.org). SWAN run in nonstationary mode from 4 April 2013 to 20 April 2013, with a spin-up phase of about 10 days before the WASS experiment.

For the sake of comparison, at the position and time of the WASS acquisition onboard the R/V "Urania", the simulated frequency–direction spectrum $S(f, \theta)$ was saved and transformed in wavenumber coordinates (left panel of Fig. 13) according to(28)

$$S(k,\theta)=S(f,\theta)\frac{df}{dk}$$

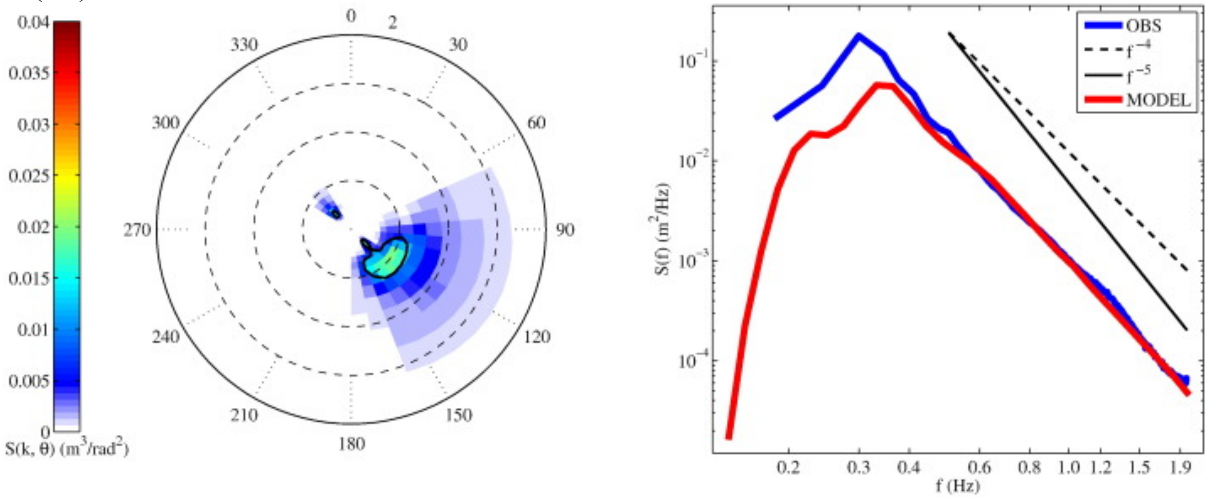

Fig. 13. (left panel) Simulated wavenumber–direction spectrum of the sea surface elevation field; directions of wave propagation are measured clockwise from north. (right panel) Omnidirectional frequency spectra derived from WASS data (OBS) and numerical simulation (MODEL). In the right-panel, the black dashed and solid lines are reference spectral slopes proportional to f^{-4} and f^{-5}, respectively.

Also, the simulated omnidirectional frequency spectrum expressed as(29)

$$S(f)=\int_{-\pi}^{\pi}S(f,\theta)d\theta$$

has been compared (right panel of Fig. 13) to the equivalent spectrum (Fig. 10) derived from stereo data using the conversion (26) between $S(k)$ and $S(f)$. With reference to Fig. 13, SWAN computed a sea state with $H_{m0} = 4\ m_0 = 0.44$ m. The difference between observed and simulated wave energies are likely due to the wind conditions that were used to force SWAN.

Indeed, during the WASS experiment and compared to observations, COSMO-I7 furnished wind conditions slightly weakened (U_{10} = 6.0 m/s). The wind forcing effect is visible in the right panel of Fig. 13 where observed and simulated energy levels agree in the equilibrium range after the spectra peak, which, however, the simulated spectrum has shifted toward smaller periods because of the aforementioned wind conditions. Moreover, the simulated directional spectrum shows two distinct spectral peaks, which correspond to a primary (θ = 125°N) and a secondary sea state (θ = 315°N). In the stereo data processing the latter is masked (see Fig. 9) given the aforementioned directional ambiguity of the 2-D Fourier transform in the (k_x, k_y)- space.

4.3. Onboard wave observations

At present, very few instrumentations are available that provide in quasi real-time the wave conditions observed from vessels underway at sea. In these conditions, we claim that accurate wave data can be gathered onboard using a stereo system. In fact, at each instant t_i of the stereo sequence, the 3-D wave field (either on the *sea* or *world* reference system) permits an estimation of the local severity of the sea state. As a matter of fact, the total wave energy S_{TOT} scales with the variance of the sea surface elevation field as(30)STOT~Eη–Eη2

The square root of the variance, i.e. the standard deviation of the sea surface elevation, is a vertical scale for wave heights, and permits, among others, to estimate the significant wave height, as in Eq. (12). Notwithstanding, as shown in Section 3.1, a large number of waves is required on average within each 3-D wave fields to recover accurately the variance (30) at each time of the sequence. This is not always the case for a stereo application, especially when a limited number of waves is included within the observed sea surface area.

For large sea surface areas, hence, even though instantaneously the mean sea plane may be correctly estimated, the estimate of variance can be biased, as shown in Section 3.1.1. Operationally, this limitation can be overcome using the 3-D wave fields while they evolve over time. Therefore, the significant wave height H_s can be approximated at a given instant in time ($t = t_i$) in the following ways:

• The standard deviation of the 3-D field $\eta_i := \eta(x_s, y_s; t = t_i) - \mathrm{E}\{\eta(x_s, y_s; t = t_i)\}$ is used to compute an instantaneous value of H_s as

(31)Hs,i=4Eηi21/2

• The variance of the sea state at $t = t_i$ is computed using the space-time wave field gathered from the onset t_0 of the stereo sequence, i.e. $\eta_e := \eta(x_s, y_s; t \in [t_0, t_i]) - \mathrm{E}\{\eta(x_s, y_s; t \in [t_0, t_i])\}$. The significant wave height is thus given by

(32) $$H_{s,e}=4E{\eta_e^2}^{1/2}$$

The latter approximation is more accurate as the severity of the sea state is retrieved from a time series of evolving 3-D wave fields. In general, the longer the time series (provided that the wave conditions are stationary) the more accurate the significant wave height $H_{s,e}$. With reference to the stereo data described earlier in Section 3.2, $H_{s,e}$ reaches a stable value (difference of few percent) after some tens of wave periods (Fig. 14), whereas the values of $H_{s,i}$ are oscillating and ranging between 0.55 m and 0.87 m, as $H_{s,i}$ is strongly dependent (as specified earlier in Section 3.1.1) on the elevations of the wave packets that pass within the stereo-camera FOV.

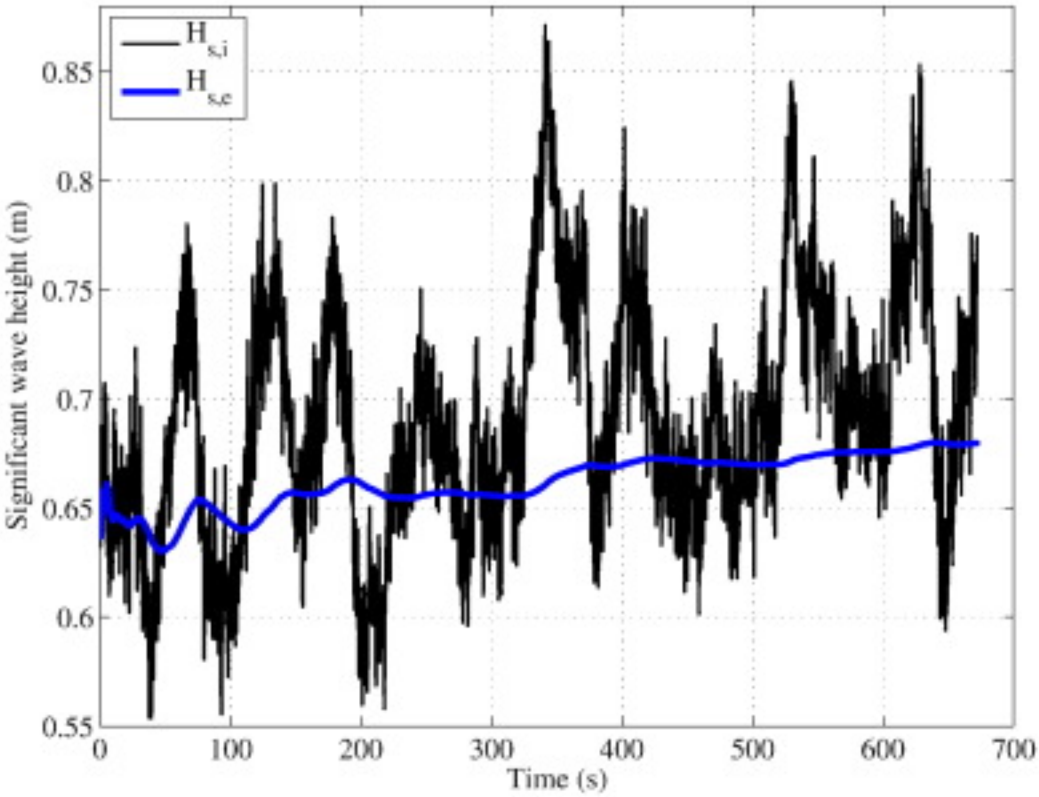

Fig. 14. Time evolution of the significant wave height computed using stereo data acquired onboard the R/V "Urania" (Section 3.2). The significant wave height is estimated by means of each individual 3-D wave field ($H_{s,i}$) and of the entire space–time wave field ($H_{s,e}$).

We would remind that the procedure proposed to estimate on board the sea state severity is not strictly valid in case of limited stereo-camera FOV on the sea surface, insofar as the mean sea plane estimation can be biased. This condition must be further investigated, and, in any case, additional information (e.g. the horizon inclination or the cameras motion from an external unit) is desirable to compensate for the vessel's movements.

5. Final remarks and conclusions

In the context of sea surface wave measurements, this paper has been motivated by the demand for transferring to moving structures the state-of-the-art technology of stereo wave imaging. Indeed, calibration procedures and computational pipelines have now reached a reliability level such that the installation and use of stereo cameras to vessels or floating platforms have become feasible. In this context, nonetheless, special care is required to map the 3-D wave fields onto a reference system with *x*- and *y*-axis lying on the mean sea plane. Once transformed to realistic wave data, stereo results can broaden the present sources of wave observations. This can be beneficial for many scientific and engineering aspects, which have been discussed. Main conclusions of the study can be summarized as follows:

• To operate on a moving platform, we claim that the stereo rig has to be adequately calibrated. Indeed, like most photogrammetric applications, an accurate calibration of the optical acquisition machinery is required. However, for practical applications, we have here suggested a calibration procedure apt to be performed in an uncomfortable environment in which it may be unfeasible to take apart or even physically access the device.

• The transformation of wave data from the *camera* to the *sea* reference system has been here discussed. Results recommend that at least about sixteen spatial waves have to be included on average within each 3-D sea surface elevation field to derive a realistic estimate of the mean sea plane, and to compute H_s with mean variability smaller than about ± 10%. The use of smaller fields of view is still possible, provided an uncertainty is tolerated. In the study the extent of such an error is evaluated using synthetic and observed space–time wave data.

• Practical uses of stereo wave imaging on moving vessels have been proposed. We have firstly identified the importance of collecting wave data from ships of opportunity in different sea conditions. Also, stereo data bring real added value compared to the existing instruments as they provide a space–time ensemble of the wavy seas. These data permit to assess unexplored behavior of the sea waves (e.g. the wave maxima over a sea area) and they can be used as a ground truth for validation of numerical wave models. It is worth of mentioning that stereo wave fields can also be fruitful for navigation purposes, as, once collected in an operational chain, they provide data to estimate the severity of the sea state.

Acknowledgments

The authors gratefully acknowledge the funding from the Flagship Project RITMARE — The Italian Research for the Sea — coordinated by the Italian National Research Council (CNR) and funded by the Italian Ministry of Education, University and Research (MIUR) within the National Research Program 2011–2015. Special thanks are given to the captain and crew of the R/V "Urania" for their help during the cruise, and Dr. Mauro Bastianini (CNR-ISMAR) for WASS deployment on the "Acqua Alta" platform. We are grateful for the comments from Dr. Paul C. Liu and one anonymous reviewer.

References

Adler and Taylor, 2007 R.J. Adler, J.E. Taylor **Random Fields and Geometry** Springer, New York (USA) (2007) (448 pp.)

Albarelli et al., 2010 A. Albarelli, E. Rodolà, A. Torsello **Robust camera calibration using inaccurate targets** Proceedings of the British Machine Vision Conference 2010, British Machine Vision Association (2010), pp. 16.1-16.10

Albarelli et al., 2012 A. Albarelli, E. Rodolà, A. Torsello **Imposing semi-local geometric constraints for accurate correspondences selection in structure from motion: a game-theoretic perspective** Int. J. Comput. Vis., 97 (2012), pp. 36-53

F. Ardhuin, E. Rogers, A. Babanin, J.-F. Filipot, R. Magne, A. Roland, A. Van Der Westhuysen, P. Queffeulou, J.-M. Lefevre, L. Aouf, F. Collard**Semi-empirical dissipation source functions for ocean waves: part I, definition, calibration and validation** J. Phys. Oceanogr., 40 (2010), pp. 1917-1941

M.L. Banner, A.V. Babanin, I.R. Young**Breaking probability for dominant waves on the sea surface** J. Phys. Oceanogr., 30 (2000), pp. 3145-3160

M.L. Banner, X. Barthelemy, F. Fedele, M. Allis, A. Benetazzo, F. Dias, W.L. Peirson **Linking reduced breaking crest speeds to unsteady nonlinear water wave group behavior** Phys. Rev. Lett., 112 (114502) (2014), pp. 1-5

M.L. Banner, I.S.F. Jones, J.C. Trinder **Wavenumber spectra of short gravity waves**
J. Fluid Mech., 198 (1989), pp. 321-344

F. Barbariol, A. Benetazzo, S. Carniel, M. Sclavo **Space–time wave extremes: the role of Metocean forcings** J. Phys. Oceanogr., 45 (2015), pp. 1897-1916

A. Baxevani, I. Rychlik**Maxima for Gaussian seas** Ocean Eng., 33 (2006), pp. 895-911

H. Bay, A. Ess, T. Tuytelaars, L. Van Gool **SURF: speeded up robust features**
Comput. Vis. Image Underst., 110 (2008), pp. 346-359

A. Benetazzo **Measurements of short water waves using stereo matched image sequences** Coast. Eng., 53 (2006), pp. 1013-1032

A. Benetazzo, F. Barbariol, F. Bergamasco, A. Torsello, S. Carniel, M. Sclavo **Observation of extreme sea waves in a space–time ensemble** J. Phys. Oceanogr., 45 (2015), pp. 2261-2275

A. Benetazzo, F. Fedele, G. Gallego, P.-C. Shih, A. Yezzi **Offshore stereo measurements of gravity waves** Coast. Eng., 64 (2012), pp. 127-138

P. Boccotti Wave Mechanics for Ocean Engineering (2000) (Oxford, 496 pp.)

N. Booij, R.C. Ris, L.H. Holthuijsen**A third-generation wave model for coastal regions: 1. Model description and validation**
J. Geophys. Res., 104 (1999), pp. 7649-7666

G. Bradski, A. Kaehler
Learning OpenCV: Computer Vision With the OpenCV Library (2008).

A. Brandt, J.L. Mann, S.E. Rennie, A.P. Herzog, T.B. Criss**Three-dimensional imaging of the high sea-state wave field encompassing ship slamming events** J. Atmos. Ocean. Technol., 27 (2010), pp. 737-752

M. Cavanie, M. Arhan, R. Ezraty**A statistical relationship between individual heights and periods of Strom waves**
Proc. Conf. Behav. Offshore Struct., 2 (1976), pp. 235-241

S. de Vries, D.F. Hill, M.A. de Schipper, M.J.F. Stive**Remote sensing of surf zone waves using stereo imaging**
Coast. Eng., 58 (2011), pp. 239-250

F. Fedele**Space–time extremes in short-crested storm seas**
J. Phys. Oceanogr., 42 (2012), pp. 1601-1615

F. Fedele, A. Benetazzo, G. Gallego, P.-
C. Shih, A. Yezzi, F. Barbariol, F. Ardhuin**Space–time measurements of oceanic sea states** Ocean Model., 70 (2013), pp. 103-115.

G. Gallego, A. Yezzi, F. Fedele, A. Benetazzo**A variational stereo method for the three-dimensional reconstruction of ocean waves**
IEEE Trans. Geosci. Remote Sens., 49 (2011), pp. 4445-4457

J. Gemmrich, C. Garrett**Unexpected waves**
J. Phys. Oceanogr., 38 (2008), pp. 2330-2336

R.I. Hartley, A. Zisserman
Multiple View Geometry in Computer Vision (2004)

K. Hasselmann, T.P. Barnett, E. Bouws, H. Carlson, D.E. Cartwright, K. Enke, J.A. Ewing, H. Gienapp, D.E. Hasselmann, P. Kruseman, A. Meerburg, P. Müller, D.J. Olbers, K. Richter, W. Sell, H. Walden **Measurements of wind-wave growth and swell decay during the Joint North Sea Wave Project (JONSWAP)**
Deutches Hydrogr. Inst., A8 (1973), pp. 1-95

H. Hirschmüller **Stereo processing by semiglobal matching and mutual information**
IEEE Trans. Pattern Anal. Mach. Intell., 30 (2008), pp. 328-341

L.H. Holthuijsen**Waves in Oceanic and Coastal Waters**
Cambridge University Press (2008)
(387 pp.)

P.A. Hwang, D.W. Wang, E.J. Walsh, W.B. Krabill, R.N. Swift**Airborne measurements of the wavenumber spectra of ocean surface waves. Part I: spectral slope and dimensionless spectral coefficient**
J. Phys. Oceanogr. (2000), pp. 2753-2767

B. Jähne**Spatio-temporal image processing: theory and scientific applications**
Lect. Notes Comput. Sci. (1993), p. 751
(Springer, 214 pp.)

Jähne, K. Riemer **Two-dimensional wave number spectra of small-scale water surface waves**
J. Geophys. Res., 95 (1990), pp. 11531-11546.

V. Kosnik, V.A. Dulov**Extraction of short wind wave spectra from stereo images of the sea surface**
Meas. Sci. Technol., 22 (2011), pp. 1-9, Article 015504.

E. Krogstad, J. Wolf, S.P. Thompson, L.R. Wyatt **Methods for intercomparison of wave measurements**

Coast. Eng., 37 (1999), pp. 235-257

F. Leckler**Observation et modélisation du déferlement des vagues**
Ph.D. Thesis
Université Européenne de Bretagne, Ecole doctorale des Sciences de la Mer, Brest, France (2013)

F. Leckler, F. Ardhuin, C. Peureux, A. Benetazzo, F. Bergamasco, V. Dulov**Analysis and interpretation of frequency–wavenumber spectra of young wind waves**
J. Phys. Oceanogr., 45 (2015), pp. 2484-2496

P.C. Liu**Contemplating ocean wave measurements**
Int. J. Geosci., 04 (2013), pp. 229-233

M.S. Longuet-Higgins**On the statistical distribution of the heights of sea waves**
J. Mar. Res., 11 (1952), pp. 245-265

M.S. Longuet-Higgins**The effect of non-linearities on statistical distributions in the theory of sea waves**
J. Fluid, 17 (1963), pp. 459-480

M.S. Longuet-Higgins**On the joint distribution of the periods and amplitudes of sea waves**
J. Geophys. Res., 80 (18) (1975), pp. 2688-2694

Y. Ma, S. Soatto, J. Kosecka, S.S. Sastry**An Invitation to 3-D Vision: From Images to Geometric Models**
(2004)

R. Miche **Mouvements ondulatoires de la mer en profoundeur constante ou Decroissante**
Ann. Ponts Chaussees, 121 (1944), pp. 285-318

A.S. Mironov, V.A. Dulov**Detection of wave breaking using sea surface video records**
Meas. Sci. Technol., 19 (2008), p. 015405

A.S. Mironov, M.V. Yurovskaya, V.A. Dulov, D. Hauser, C.A. Guérin**Statistical characterization of short wind waves from stereo images of the sea surface**
J. Geophys. Res., 117 (2012), Article C00J35

J.C. Nieto Borge**Detection of ocean wave groupiness from spaceborne synthetic aperture radar**
J. Geophys. Res., 109 (2004), Article C07005

D. Nister**An efficient solution to the five-point relative pose problem**
IEEE PAMI, 26 (2004), pp. 756-770

M. Onorato, A.R. Osborne, M. Serio, D. Resio, A. Pushkarev, V.E. Zakharov, C. Brandini**Freely decaying weak turbulence for sea surface gravity waves**
Phys. Rev. Lett., 89 (2002), p. 144501

O.M. Phillips**On the response of short ocean wave components at a fixed wavenumber to ocean current variations**
J. Phys. Oceanogr., 14 (1984), pp. 1425-1433

W.J. Pierson, G. Neumann, R.W. James, Practical methods for observing and forecasting ocean waves by means of wave spectra and statistics, Washington, U.S. Navy Hydrographic Office (1955), p. 284

V.I. Piterbarg**Asymptotic methods in the theory of Gaussian processes and fields**
Translations of Mathematical Monographs (1996)
(206 pp.)

J.J. Rodriguez, J.K. Aggarwal**Stochastic analysis of stereo quantization error**
IEEE Trans. Pattern Anal. Mach. Intell., 12 (1990), pp. 467-470

L. Romero, W.K. Melville**Airborne observations of fetch-limited waves in the Gulf of Tehuantepec**
J. Phys. Oceanogr., 40 (2010), pp. 441-465

L. Romero, W.K. Melville**Spatial statistics of the sea surface in fetch-limited conditions**
J. Phys. Oceanogr., 41 (2011), pp. 1821-1841

A. Russo, A. Coluccelli, S. Carniel, A. Benetazzo, A. Valentini, T. Paccagnella, M. Ravaioli, G. Bortoluzzi**Operational Models Hierarchy for Short Term Marine Predictions: The Adriatic Sea Example**
OCEANS13 MTS/IEEE, Bergen (Norway) (2013), pp. 1-6

A. Schumacher **Stereophotogrammetrische Wellenaufnahmen**
Wiss. Ergeb. Dtsch. Atlant. Exped. Forschungs Vermessung. Meteor (1939)

M. Schwendeman, J. Thomson **A horizon-tracking method for shipboard video stabilization and rectification**
J. Atmos. Ocean. Technol., 32 (2015), pp. 164-176

S. Sclavo, F. Barbariol, F. Bergamasco, S. Carniel, A. Benetazzo **Italian seas wave extremes: a preliminary assessment**
Rend. Fis. Acc. Lincei, 26 (1) (2015), pp. 25-35

K.T. Shum, W.K. Melville **Estimates of the joint statistics of amplitudes and periods of ocean waves using an integral transform technique**
J. Geophys. Res., 89 (1984), pp. 6467-6476

M.J. Tucker, P.G. Challenor, D.J.T. Carter **Numerical simulation of a random sea: a common error and its effect upon wave group statistics**

Appl. Ocean Res., 6 (1984), pp. 118-122

WAFO Group**WAFO — A MATLAB Toolbox for Analysis of Random Waves and Loads, Version 2.5**
Mathematical Statistics, Lund University (2011)

D. Xu, X. Li, L. Zhang, N. Xu, H. Lu**On the distributions of wave periods, wavelengths, and amplitudes in a random wave field**
J. Geophys. Res. C: Oceans, 109 (2004), pp. 1-16

V.E. Zakharov, N.N. Filonenko**Energy spectrum for stochastic oscillations of the surface of a liquid**
Sov. Phys. Dokl., 11 (1967), pp. 881-883

C. Zappa, M. Banner, H. Schultz, A. Corrada-Emmanuel, L. Wolff, J. Yalcin**Retrieval of short ocean wave slope using polarimetric imaging**
Meas. Sci. Technol., 055503 (2008), pp. 1-13